UNIVERSITY OF OKLAHOMA
GRADUATE COLLEGE

INFLUENCE OF INTERFACIAL RHEOLOGICAL PROPERTIES ON THE STABILITY OF PICKERING FOAMS

A THESIS
SUBMITTED TO THE GRADUATE FACULTY
In partial fulfillment of the requirements for the
Degree of
MASTER OF SCIENCE

By
NICK BROWN
Norman, Oklahoma
2022

INFLUENCE OF INTERFACIAL RHEOLOGICAL PROPERTIES ON THE STABILITY OF PICKERING FOAMS

A THESIS APPROVED FOR THE
SCHOOL OF CHEMICAL, BIOLOGICAL AND MATERIALS ENGINEERING

BY THE COMMITTEE CONSISTING OF

Dr. Sepideh Razavi, Chair
Dr. Jeffrey Harwell
Dr. Ngoc Bui

Thesis Advisor
Dr. Sepideh Razavi

Author
Nick Brown

Influence of Interfacial Rheological Properties on the Stability of Pickering Foams

ABSTRACT

This work is aimed at gaining a fundamental understanding of the role of interfacial phenomena in foam stability. We have investigated the properties of Pickering foams, stabilized with fumed and spherical colloidal silica nanoparticles, and studied the impacts of particle attributes on the resulting properties such as bubble microstructure, foam liquid content, and foam half – life. We have examined the microstructure of analogue particle – laden interfaces and probed their response to applied deformations via both interfacial dilatational and shear rheology measurements. While the overall foam heights and microstructure remain similar for both particle types used, differences are observed in their interfacial shear and dilatational rheological measurements. Foams stabilized with fumed silica particles are able to resist liquid drainage to a higher degree, as captured by a plateaued reduced osmotic pressure over time, whereas the reduced osmotic pressure for the spherical particle – stabilized foams increased slowly over time. With regards to rheology, the interfacial network formed by spherical silica particle had slightly larger values of elastic moduli (E') than the fumed silica network. However, interfaces coated with fumed silica particles, undergoing dilational deformations, retained a particle network over a broader range of dilational strain compared to spherical particles. In shear mode, the interfacial networks formed by the spherical particles have higher storage moduli (G') compared to those obtained from fumed particles, whereas the critical shear strain corresponding to the yield point is larger for the fumed particle networks. Our findings demonstrate that while both fumed and spherical silica particles are able to stabilize the air/water interface and make long – lasting foams, the resulting Pickering foams are markedly different with respect to their network properties and resistance to various destabilization mechanisms.

Keywords: particle – stabilized foams; interfacial rheology; destabilization mechanisms; nanoparticles; fluid interfaces

TABLE OF CONTENTS

1 INTRODUCTION 1
2 BACKGROUND 3
  2.1 Pickering Foams..4
  2.2 Mixed Systems of Particles and Surfactants..7
  2.3 Bulk Rheology 8
  2.4 Interfacial Rheology..11
3 MATERIALS AND METHODS..15
  3.1 Materials 15
  3.2 Colloidal Particle Modification..15
  3.3 Particle Characterization – Wettability..16
  3.4 Particle Characterization – Size and Charge..16
  3.5 Foam Generation 17
  3.6 Foam Characterization 18
  3.7 Drop Shape Tensiometry 20
  3.8 Langmuir Trough Measurements 22
  3.9 Shear Rheology Experiments..23
  3.10 Particle Characterization – Microscopy..24
  3.11 Image Analysis..25
  3.12 Viscosity Measurements..28
4 PARTICLE & SOLUTION CHARACTERIZATION..29
  4.1 Wettability..29
  4.2 DLS & Zeta Potential..30
  4.3 SEM & AFM..32
  4.4 Bulk Solution Viscosity 36
5 FOAM STABILITY 39
  5.1 Foam Height & Half – life 39
  5.2 Osmotic Pressure 46
  5.3 Microstructure..52
  5.4 Mixed Systems: Surfactant & Particles 54

6 INTERFACIAL DILATIONAL RHEOLOGY 61
6.1 Droplet and Langmuir Trough Compressions 61
6.2 MSA and Colloidal Dilational Elastic Moduli..62
6.3 Frequency and Concentration Dependence 65
6.4 Dilational Characteristics of the Interface and Foam Stability..........................67
7 INTERFACIAL SHEAR RHEOLOGY 70
7.1 Amplitude Sweeps and Curve Fitting 70
7.2 Frequency Sweeps and Frequency Dependence 72
7.3 Surface Coverage Calculations 74
7.4 Interfacial Shear Rheology Properties 77
8 CONCLUSIONS AND OUTLOOK...80
REFERENCES 83
APPENDIX I 94

LIST OF FIGURES

3.1 Frontal view of the Dynamic Foam Analyzer 100 (DFA100) (left); Liquid content module with electrodes (right). 19

3.2 Drop shape Tensiometer setup (left) and the needle used for pendant drop experiments (right). 20

3.3 Langmuir trough (left) alongside the inverted microscope (right). 22

3.4 Ribbon trough with DWR setup (left). Red circles indicate where the particle deposition was carried out. Diagram of the DWR (right). 23

3.5 Schematic of particle monolayer deposition onto a silicon wafer. 24

3.6 Image analysis of a colloidal interfacial monolayer during compression. A) Base image without corrections; B) Image after manually thresholding; C) Image after Gaussian blur, Enhance Contrast, and Find Edges performed; D) Image C after Sharpening, Multiply, and Make Binary were performed. 27

4.1 Contact angle measurements carried out using a water droplet deposited onto a monolayer of (a) colloidal, (b) LSA, (c) MSA particles on a glass substrate. 30

4.2 An example of DLS Intensity graphs obtained for MSA particles. 32

4.3 SEM images of MSA (left) and DMDCS treated colloidal particles (right). 33

4.4 MSA & colloidal particles side by side comparison. 34

4.5 AFM images for colloidal particles (top) along with height graphs of the respective image (bottom). 35

4.6 4.6: AFM images for MSA particles (top) along with height graphs of the respective measured area (bottom). 36

4.7 Comparison of Cone & Plate method (left) and the Bob & Cup method (right) for viscosity measurements carried out on MSA particle dispersions at various particle concentrations. 38

4.8 Viscosity trials of MSA fumed (left) and colloidal (right) particle dispersions via cone & plate methodology. 38

5.1 Total height (foam + solution) for systems stabilized with different stabilizing agents (left); Normalized height (H/H0) for the same systems stabilized with different agents (right). 40

5.2 Foam height and drained liquid height as a function of MSA fumed silica particle concentrations of (a) 0.5wt%, (b) 1.0wt.%, and (c) 2.0wt.%; Inset is a closer look at the drained liquid height over a smaller timescale to highlight drainage over time 41

5.3 Foam half – life for MSA fumed silica particle – stabilized foams as a function of concentration. 42

5.4 Foam height and liquid height for 6.0wt.% colloidal – particle stabilized foams over 3600s. 44

5.5 Change in the osmotic pressure with time for foams generated from 0.5 CMC SDS solutions. 46

5.6 Osmotic Pressure as a function of time for 0.5 CMC SDS foam triplicates versus the overall foam height; (a) Full graph without removal of sensor data outside of foam height limits; (b) correcting the graph (a) to remove the calculated osmotic pressure points that reside outside the actual foam height data. 48

5.7 Osmotic pressure versus time for MSA particle – stabilized foam trials, with respect to foam height. (a) 0.5wt.%, (b) 1.0wt.%, and (c) 2.0wt.% MSA particles...........50

5.8 Osmotic pressure versus time for colloidal particle – stabilized foam trials, with respect to foam height (open square symbol) at 6.0wt.% colloidal particles.........52

5.9 Comparison of bubble counts between 0.5 CMC SDS (black square) and 2.0wt.% MSA (red circle). The camera is in 1st position (~285mm2 total area) 53

5.10 Comparison of microstructures captured for SDS and Pickering foams. Row 1) SDS – stabilized foams at 60, 600, 1800, and 3600s respectively; Row 2) MSA fumed silica particle – stabilized foams at 60, 600, 1800, and 3600s respectively; Row 3) Colloidal particle – stabilized foams at 60, 600, 1800, and 3600s respectively. ..54

5.11 Foam height of (a) SDS – only solutions and (b) 2.0wt.% fumed silica and SDS solutions at varying SDS concentrations normalized by the CMC values. 56

5.12 Osmotic pressure versus time for foams stabilized with mixed fumed silica/surfactant solutions at varying SDS concentration of (a) 0.5 CMC, (b) 1.0 CMC, and (c) 2.0 CMC; in all systems, the MSA particles are present at 2.0wt.%. 57

5.13 Rate of Ostwald ripening for SDS – only (a) and mixed systems (b); rate of coalescence for SDS – only (c) and mixed systems (d). 60

6.1 Compression isotherms obtained from droplet tensiometry for (a) 1.5mg MSA and (b) 3.75mg colloidal particles. Langmuir trough compression isotherms for (c) fumed and (d) colloidal particles.. 62

6.2 Surface tension and surface area curves with time, δ represents the phase angle between the two curves. 63

6.3 Dilational elastic modulus E' for interfacial networks of fumed silica (left) and colloidal silica (right) particles. The dark blue line represents the Gibbs stability criterion $E' > \gamma/2$ 65

6.4 Dilational elastic modulus obtained at various surface pressures for interfacial network of MSA particles as a function of the initial solution concentration deposited on the pendant droplet surface. 66

6.5 The frequency dependence of the dilational elastic moduli for interfacial networks of MSA (top) and colloidal (bottom) particles as a function of surface pressures. 67

6.6 MSA particle shell remains after foam trial completion. 69

7.1 Amplitude sweeps performed at 1Hz for interfacial network of MSA (left) and colloidal (right) particles. 71

7.2 Fitting of critical parameters from the amplitude sweep data for a colloidal trial. G'_c is the critical storage modulus at which the curves tend towards the non-linear regime. γ_c is the critical strain at which G'_c takes place. 71

7.3 G' and G'' data and the corresponding fits obtained from interfacial shear frequency sweeps spanning from 5 – 35 mN/m surface pressures, at .005% over .02 – 10 Hz for (a), (c) fumed and (b), (d) colloidal particle networks. 74

7.4 Image conversion and analysis for particle coverage and fractal dimensions. (a) Base image; (b) thresholded black & white of the base image; (c) thresholded base image run through FracLac for fractal box counting; (d) zoomed in image of the boxes on the base image. 75

7.5 Calculated surface coverage for fumed and colloidal interfaces during compression as a function of surface pressure. MSA coverage calculated backwards from the inflection point, and colloidal coverage calculated from image analysis obtained from imaging the interface at each surface pressure listed (left); Surface coverages calculated backwards from the inflection point for both interfaces (right). 77

7.6 (a) critical strain, (b) critical elastic modulus at yield, and (c) yield stress of the interfacial networks as a function of the particle surface coverage for both networks formed by the colloidal and fumed particles. 79

A.1 Comparison of mixed system foams. Row 1) SDS at 60, 600, 1800, and 3600s respectively; Row 2) MSA at 60, 600, 1800, and 3600s respectively; Row 3) Mixed MSA & 0.5 CMC SDS at 60, 600, 1800, and 3600s respectively. 94

A.2 SDS elastic modulus values (red points), with regards to the Gibbs stability criterion (blue line). 95

A.3 Static (left) and dynamic (right) Wo values for the same MSA compression data set. 97

ACKNOWLEDGEMENTS

I would like to thank Dr. Razavi for her endless hours of help and instruction over this past year as I worked towards this thesis, as well as her help prior during my undergraduate time within her lab. Without her help, I would not have learned the skills and abilities required of me to conduct this research and to understand the minutia of this field to the degree that I have. I would also like to thank my fellow lab members: Elton Lima Correia, Siddharth Thakur, Ashley Copelin, Matthew Webb, Emma Shields, Eduarda Barros de Oliveira, as well as past members Alec de la Pena and Aanahita Ervin. Their help in lab and their insight on many of the undertakings required for this research cannot be understated. Lastly, I would like to thank my friends and family for supporting me through this process and listening to my research problems regardless of if they knew what I was discussing or not.

1. Introduction

Particle – stabilized (i.e., Pickering) foams have recently become a topic of interest due to their ability to remain stable and last longer than foaming agents such as surfactants, which has allowed them to be utilized in many applications and at operating conditions foams would typically not be able to withstand. While a body of research has been carried out to investigate the impact of particle attributes on properties of the resulting particle – laden interfaces, such as elasticity, collapse modes under applied stresses, and mechanical stability, less is known on the linkage between these interfacial characteristics and the Pickering foam properties. In section 2, we will review the studies available in the literature conducted on both particle – stabilized foam characteristics as well as the bulk and interfacial rheological properties of solutions and interfaces decorated with particles. In section 3, we will introduce the materials and methodologies utilized in our experimental studies. The characteristics of particles under study such as wettability, hydrodynamic diameter, particle impact on solution preparation, and bulk viscosity of particle samples will be discussed in section 4. Methods used to characterize the overall resistance of foams to destabilization mechanisms will be introduced in section 5 and the impacts of particle type, concentration, and surfactant addition on foam stability will be elucidated. The dilational rheological properties of interfaces populated by fumed and spherical colloidal nanoparticles will be discusses in section 6, as well as the effects of frequency and concentration, which will be tied back to the previously observed foam stability. Lastly, in section 7, the shear rheological limits will be calculated for our systems and the characteristics of the interface will be extracted via amplitude and frequency sweeps resulting in information regarding critical properties tied to foam stability. Overall, we attempt to elucidate the impact of particle attributes on the microstructure formed at the interface and the dilatational and shear rheology of such particle – laden interface. By establishing these connections between the rheological properties of the interface and the macroscopic characteristics of the Pickering foams, such as their stability, a framework can be achieved and applied for engineering interfacial systems with a desirable set of properties.

2. Background

Particle – stabilized (i.e., Pickering) foams have shown applicability in various areas ranging from decontamination of nuclear facilities to the froth flotation of minerals.[1-10] Foams are promising candidates for applications in the petroleum industry including enhanced oil recovery[11-13] hydraulic fracking of unconventional oil and gas resources[14, 15] and gas well deliquification[16] because their low liquid content causes less damage in water sensitive formations and reduces the water consumption and disposal in subsurface resource recovery applications. Their applicability in part is due to their ability to withstand destabilization mechanisms such as coalescence[17, 18] and Ostwald ripening[19-22], and to remain stable under high temperature[23-25] and high salinity[26-30] conditions compared to other foaming agents such as surfactants.[31-34] Pickering foams are of great potential due to the large desorption energy of single particles from the interface (ΔE) that can be estimated as follows:

$$\Delta E = \gamma_w \pi R^2 (1 \pm \cos\theta)^2 \qquad (1)$$

where γ_w is the air/water surface tension, R is the particle radius, and θ is the particle 3 – phase contact angle at the interface. As an example, for a particle with nominal size of 250nm and neutral wettability (i.e., $\theta = 90°$), the interfacial binding energy is $\sim 10^6 k_B T$, where $k_B T$ is the thermal energy. Due to the large desorption energy in such a system, the particles are irreversibly adsorbed onto the interface unlike surfactants which can be reversibly exchanged between the interface and the bulk solution.

2.1 Pickering Foams

A number of key particle attributes are reported to impact the stability and properties of Pickering foams. Particle concentration has been shown to improve the foam half – life and foam volume compared to those formed solely by foaming agents like surfactants.[6, 33-38] For example, Binks et al.[33] showed that for an air/water system, an increase in the concentration of particles (6µm at 25ºC, Expancel® micro – spherical plastic made of a 2µm acrylic copolymer shell encapsulating isobutane) from 0.5 – 10wt.% caused the average bubble radius to initially increase from 100µm to 350µm (0.5 – 7.0wt.%), and then subsequently remain stable at around 200µm with 10wt.% particles in the system. This was attributed to low stabilization against coalescence in foams prepared with lower particle concentrations due to partial particle coatings which caused the bubble size to increase. With increased particle concentration, the enhanced stabilization against coalescence led to bubble sizes that remained uniform after generation. Not only did the increased particle concentration alter the microstructure of the foam, but it also extended its half – life tremendously which led to particle – stabilized foams that lasted upwards of six months for all particle concentrations tested.

Particle size is another attribute that can impact 'foaminess', or the volume percent of air incorporated into the system, as shown by Sethumadhavan et al.[39] It was observed that by an increase in particle size at 10wt.%, the overall 'foaminess' decreased from 550% for the 8nm particles to only around 20% for 100nm particles. This was attributed to the lower effective volume fraction that can be achieved via larger particles within the lamellae, as well as a decrease in the number of particle layers that can form in the foam lamellae, which play a role in the stability of the liquid films against drainage.

Particle wettability impacts the stability of Pickering foams as it affects the position of particles at the interface and the resulting interparticle interactions. As can be seen in Eq. (1) altering the particle contact angle at the interface, affects the air/water contact area and the binding energy of the particle. Particles that occupy the largest area at the air/water interface, i.e., $\theta \sim 90°$, have shown to produce larger foam volumes and longer – lasting foams[40-43], while particles of extreme wettability, i.e., very hydrophilic ($\theta < 30°$) or very hydrophobic ($\theta > 150°$) tend to be poor foam stabilizers.[44] However, it has been shown that if the maximum capillary pressure of the foam lamellae was taken into account, then the most stable contact angle for a double particle layer was around 86° and around 71° for a single particle layer.[45] Johnston et al.[42] used hydrophobically modified fumed silica nanoparticles and observed that with a decrease in the number of silanol groups (i.e., SiOH) on the silica particle surface, and therefore an increase of the particle contact angle at the air/water interface, the particles led to foam generation with a higher initial volume. In particular, the foam height increased from ~0.65cm to ~2.3cm using hydrophobically modified particles with 70% SiOH and 35% SiOH surface groups, respectively.

Manga et al.[46] studied the effect of the pH on the wettability of latex particles (53nm) grafted with pMMA – b – pDMAEMA. It was shown that at a low pH ~ 2, an increase in the particle concentration (0.1 – 4.0wt%) had relatively low impact on the change in interfacial tension, which remained constant around 52 $\mathrm{mNm^{-1}}$. However, when the pH was varied from 2 to 10, a change in the interfacial tension was reported that was attributed to the pH sensitivity of the particle grafts. At low pH values, the grafted polymer chains are protonated and therefore cause the particle to be very hydrophilic allowing it to reside in the aqueous phase with no impact on the interfacial tension. When the pH is increased to 10, the polymer chains become deprotonated rendering the particles more hydrophobic and increasing their affinity for the interface, which leads to the observed decrease in the interfacial tension down to ~25 mNm^{-1}.

Particle anisotropy, in surface or shape, can also impact the resulting interparticle interactions at a fluid – fluid interface.[19, 41, 47-49] Karakashev et al.[50] studied how particle shape anisotropy can lead to varied foam characteristics using spherical silica nanoparticles (~11µm) and a needle – like structure sepiolite particle (~45µm). When the particle concentration was increased (from 0.01 to 2.0wt.%), the overall foam volume increased from 50mL to 70mL for those stabilized with spherical particles, whereas the needle – like particles increased the foam volume from 100mL to 180mL. The foams stabilized with 2wt.% of the needle – like particles also exhibited an increased half – life (1800s) compared to their analogue stabilized with spherical particles (500s). The improved foam stability in case of needle – like particles was attributed to their ability for formation of a stronger interfacial network in contrast with the spherical particles.

The effect of other additives present in the solution, such as electrolyte,[24, 26, 29, 42] surfactant,[6, 11, 37, 51-56] and polymer,[57-60] on the stability of Pickering foams has also been studied in the literature. For example, Kostakis et al.[61] found that when the concentration of the electrolyte was increased (from 0.5 to 3.0mM) in foams stabilized with fumed silica particles (20nm), the overall fraction of bubbles remaining over time increased and led to an enhancement in the bulk dynamic storage modulus (G') of the system (from ~2 Pa to ~8 Pa). The reduction in the Debye length with higher electrolyte concentrations enabled the formation of a more tightly packed particle network on the bubble surface, which led to an increase in the bubble resistance to destabilization as well as the viscosity of the system.

2.2 Mixed Systems of Particles and Surfactants

Mixed systems of surfactants and particles have also been investigated and a cooperative nature has been observed with regards to improving foam stability.[6, 31, 32, 47, 51, 62-66] Hu et al. [47] looked into the effects of particle size for systems of spherical silica nanoparticles (20, 100 and 500nm) with cationic cetyltrimethyl ammonium bromide (CTAB) and anionic sodium dodecyl sulfate (SDS) surfactants. It was found that not only does the particle size affect the amount of foam and the resulting half – life, the interactions between these surfactant molecules and the particles play a role in the stability of the foam. Depending on the charge of the surfactant molecules, their adsorption onto the particle surface could alter the overall characteristics of the particle and their behavior near the air/water interface. The positively charged CTAB molecules adsorb onto the surface of negatively charged silica particles, which lowered the overall negative charge of the particle and the corresponding zeta potential, which, in turn, resulted in a change of the particle wettability. For the case of negatively charged SDS surfactant molecules, the adsorption can occur with the surfactant tail facing towards the particle surface resulting in a larger negative charge on the particle and a higher particle hydrophilicity. For both surfactant species used, the overall initial foam volume decreased when particles were added. When using 0.01wt% CTAB the initial foam volume was around 500mL and decreased with decreasing particle size down to around 250mL for 20nm particles. Alternatively, when 0.01wt% SDS was utilized, the initial foam volume was around 400mL, but then decreased with increasing particle size to around 100mL for 500nm particles. The half – lives of the foam were all improved with the addition of particles but exhibited an inverse relationship with the overall foam heights, i.e., the particle size that produced the lowest amount of foam also caused the longest lasting foam. When a 1:1 weight ratio of CTAB/particles was used, the half – life was increased to around 82.5 minutes when 20nm particles were introduced compared to 67.5 minutes for just CTAB. Similarly, when a 1:1 weight ratio of SDS/particles was used, the half – life for the 500nm particles was around 60 minutes compared to 30 minutes for just SDS. Ultimately, the authors state that CTAB adsorption onto the nanoparticles caused the loss of foamability for increasing particle sizes, while for SDS they attributed the effects to the solution viscosity, which increased with decreasing sizes that led to less foamability as well. Studies on the effect of other factors such as temperature and foam fabrication techniques on the foam stability can also be found in the literature. [23, 24, 29, 56, 67, 68]

2.3 Bulk Rheology

The impact of bulk rheological properties on the stability of Pickering foams and emulsions have also been examined in the literature.[69-71] The bulk viscosity is shown to be impacted heavily when particles are introduced into the system due to their ability to interact and create a particle network.[37, 42] Vishal et al.[37] found that with increased concentration of silica nanoparticles (10nm, 0 – 0.5wt.%), the foam viscosity curves, with 0.1mM cationic hexadecyltrimethylammonium bromide (HTAB), shifted up to higher values from 1.5 – 0.01 Pa.s to 6.0 – 0.2 Pa.s for 0 and 0.5wt.% nanoparticles respectively, over the range of $1 - 100\text{s}^{-1}\ \dot{\gamma}$. The foam samples also display shear thinning behavior, which show initially that the particle networks are intact and caused resistance to flow; however, at larger shear rates the network was broken up and a lower viscosity of the solution is produced. Moreover, even with increased HTAB concentrations to 1mM and 10mM, the foam viscosities continued to shift higher with increased particle concentration, even though at 10mM HTAB the initial viscosities overall decreased to 0.15 Pa.s and 0.22 Pa.s at $1\mathrm{s}^{-1}\dot{\gamma}$ for 0 and 0.5wt.% particles respectively. The authors state that due to the differently charged species interacting, the surfactant would bind to the silica particle surface and increase its hydrophobicity. At low surfactant concentrations, they would mostly bind to the surface of the particle which enabled the particles to move towards and bind to the interface more strongly. However, when the concentration was increased above the CMC, or critical micelle concentration at which micelles begin to form, of the surfactant, the surfactants saturated the bubble films themselves, which inhibited the formation of particle networks. Ultimately, the authors state that due to the increase in the interfacial shear viscosity at the air/water interface caused by the introduction of particles at surfactant concentrations below CMC, the foams were stable for longer periods of time (200min for 0wt.%, ~1000min for 0.5wt.% at 0.1mM HTAB).

Amiri et al.[26] also illustrated the effects of particle concentration with salts and how they led to changes in the bulk rheological properties. Using strain amplitude sweep measurements, it was shown that with increasing fumed silica nanoparticle concentration (1.3 – 2.3wt.%) at .6M NaCl both the storage (G') and loss (G'') moduli increased. At the same time, the yield strain (γ_c) decreased with particle and salt concentration, i.e., while the system was more resistant to shearing with increased particle concentration, the maximum strain before collapse decreased. This was attributed to the solution being in the 'strong gel' regime, one in which the G' value increases with a positive exponent, while the yield strain decreases with a negative exponent. In the 'strong gel' regime, the fractal flocs of particles have higher elastic constants when interacting between the flocs than within the floc itself, which causes higher elastic moduli. However, the linearity limit decreased with particle concentration. Addition of NaCl up to 2.75M into the system also led to increased shear moduli for the system, which was attributed to an enhanced interparticle interactions and network formation in presence of the electrolyte.

Bose et al.[28] studied the impacts of both particle shape (spherical or fumed) as well as electrolyte concentration (0.1mM/50mM NaCl) on resultant emulsion viscosity as well as the interfacial properties of the bromohexadecane – water interface. Using spherical silica particles (D = 210 ± 10nm) it was found that at both salt concentrations the suspension exhibited Newtonian behavior, with a viscosity close to that of water. In comparison, the fumed silica particles (D = 204 ± 20nm) showed Newtonian behavior only at 0.1mM and exhibited shear thinning in presence of 50mM electrolyte. This was determined to be due to the volume filling network the fumed silica particles form, which was around 11 times larger than the spherical particles. With regards to the oscillatory strain experiments performed on the emulsions, there were key differences found between the spherical and fumed particles. The fumed particles were found to have storage moduli (G') up to two orders of magnitude larger at 50mM than the spherical particles, which illustrated the formation of the large volume filling network displayed by the viscosity trials. Overall, the fumed silica particles were better able to stabilize the emulsions than the spherical particles, due to their ability to make large volume filling networks when the interparticle interactions turn more attractive with increased salt concentrations.

2.4 Interfacial Rheology

It has been well established that when nanoparticles irreversibly adsorb to the interface, they can alter the mechanical stability[18, 72] of the interface and the rates of Ostwald ripening and coalescence. Thus, probing the rheological characteristics of an interface is pertinent to understanding the connections between particle effects at the interface and the stability of foams. Interfacial shear rheology can give insights on the elasticity[73, 74] of the interface and its resistance to deformation; it can also capture the impact that the interfacially bound particles have on the rate of Ostwald ripening[19] as well as the mode of collapse.[40, 75, 76] In tandem, interfacial dilational rheology can capture the ability of the interface to resist distortion and deformation, which are both key factors when attempting to control or in some cases completely retard coalescence in foams.[27, 77] These measurements are conducted by either expanding and contracting the interface or shearing, for dilatational and shear rheology, respectively.[78] From these tests information can be obtained that provide insight on the rheological properties such as how resistant the interface is to deformation[26, 79, 80] or the yield point at which the particle network is altered away from being strictly a monolayer. These rheological properties, much like the foam characteristics above, can be affected by particle and electrolyte concentration,[26, 28, 81] particle anisotropy,[19] and wettability.[40, 82, 83]

Zhu et al.[84] studied the dilational rheological properties of interfaces in presence of nanoparticles and surfactants in order to elucidate their roles on the stability of such interfaces. Anionic nanoparticles (28.5 ± 0.2nm) were used in tandem with the cationic surfactant Arquad 12 – 50 and were tested using pendant drop tensiometry. It was shown that in presence of the surfactant alone, the interface exhibited an $E' \sim 0 - 10$ mN/m for surfactant concentration of 0.01% and 0.1% , respectively. When 0.1% particles were added to the droplet along with 0.01% surfactant, the E' rose to around 20mN/m, and when the concentration of particles was increased to 0.3% the E' reached ~70mN/m leading to a much more elastic behavior of the interface. These E' values were tied to the Gibbs modulus, which is often used to characterize whether an interface would stabilize foam or emulsions completely, or if the resulting system would be unstable by checking whether $E' > \gamma/2$. It was observed that for the surfactant only system, all values of E' were below $\gamma/2$ resulting in poor stabilization of foams. When 0.1% of particles were added, E' was greater than $\gamma/2$ for a majority of surface pressures tested but still had some areas of predicted instability, and when 0.3% of particles were introduced, the $E' > \gamma/2$ condition was held for all surface tensions studied.

Manga et al.[46] also utilized interfacial dilational rheological techniques to characterize the pH – responsive effect of latex particles (300nm) on the interfacial tension, as discussed earlier. At lower pH values (e.g., 2), the particles were protonated and remained in the aqueous phase instead of being adsorbed onto the interface; therefore, the dilational elastic modulus E' was very low similar to a pure air/water interface. Alternatively, E' was large for the particle interface, around 120 mNm^{-1} at pH 10, which resulted in very strong stability of emulsion and foam systems that was attributed to the surface activity of the pH – sensitive particles.

To highlight the effects of particles on interfacial shear properties, Beltramo et. al[19] examined the impact of particle shape anisotropy on the interfacial shear and its connection to the bubble dissolution. Polystyrene spheres (~820nm) and ellipsoids (~2.48μm long and 0.45μm wide) were used and it was found that with an increase in the particle surface packing, (0.59 – 0.9 for spheres and 0.61 – 0.66 for ellipsoid), the yield stress of the interfacial network increased, and a higher pressure was necessary for the diffusion of gas through the interface, which highlights the link between interfacial shear properties and Ostwald ripening in foams.

Yu et al.[80] delved into the effects of subphase electrolyte concentration and surface pressure on the rheological properties of polyvinylpyrrolidone – coated silica nanoparticles (hydrodynamic diameter D_h = 52nm) at the air water interface. They found that at all salt concentrations utilized (0.01, 0.1, 0.55M) the interface displayed elastic characteristics (G' > $G"$) at surface pressures > 3mN/m with G' ranging from 0.001 Pa.m with 0.01M to 0.02 Pa.m with 0.55M, whereas the interface was viscous dominant at lower surface pressures. The critical surface pressure of the interface to switch from viscous – to elastic – dominant behavior also decreased with increasing salt concentration. The oscillation frequency dependence of the rheological properties was then determined at different surface pressures and subphase electrolyte concentrations in order to characterize the time – dependent dynamics of the particle – laden interface. At 0.5mN/m surface pressure, it was observed that the interface was viscous – dominant for each electrolyte concentration studied and that G' and $G"$ were dependent on the oscillation frequency to the first power (ω^1). When the surface pressure was increased to 2 mN/m, the samples at higher electrolyte concentrations (0.1 & 0.55M) transitioned to elastic – dominant behavior with decreased dependence of G' and $G"$ on the oscillation frequency. The G' of the 0.55M sample at 2 mN/m showed complete independence (ω^0) which signified the onset of the glass state of the interface. At the highest surface pressure analyzed (4mN/m) all G' values were independent of oscillation frequency, however the G'' still showed a small dependence which suggested that viscous forces were still influencing the interfacial behavior.

3. Materials and Methods

3.1 Materials

All experiments described utilized hydrophobically modified fumed silica (fumed) particles TS – 610 (LSA) and TS – 622 (MSA) (CAB – O – SIL®), as well as colloidal spherical (colloidal) particles (Fiber Optic Center Inc.). TS – 610 has a low surface area of 125 ± 20 m^2g^{-1}, while the TS – 622 has a moderate surface area of 195 ± 20 m^2g^{-1} and the colloidal particles have a nominal surface area of 10.5 m^2g^{-1}. Both TS – 610 and TS – 622 have primary silica nanoparticle diameters of approximately 25nm. The hydrodynamic diameter of the TS – 610 and TS – 622 were measured to be 189 ± 15.7 nm and 196 ± 70.1 nm respectively, using Dynamic Light Scattering (Brookhaven Instruments, NanoBrook Omni DLS) technique. The colloidal particles have a nominal diameter of 250nm, a diameter of 283 ± 28.0nm measured using a Scanning Electron microscope (NEON Field – Emission Scanning Electron Microscope, Zeiss), and a hydrodynamic diameter of 322.3 ± 120.9nm. All particle types are hydrophobically modified with dimethyldichlorosilane (DMDCS).[75] Anhydrous ethanol, chloroform, and cyclohexane were purchased from Fischer Scientific, which were utilized in sample preparation and colloidal nanoparticle silanization[75]. Deionized (DI) water was generated via Milli – Q® IQ 7000 Ultrapure Lab Water System (Millipore Sigma).

3.2 Colloidal Particle Modification

The colloidal nanoparticles were modified using DMDCS following the procedure by Razavi et al.[75]. In brief, 1g of the colloidal particles were oven dried overnight at 60ºC and placed in 10mL of cyclohexane. Then 121.7µL of DMDCS was added to the solution

(10^{-1} M), which was sonicated in a bath sonicator (Fisherbrand™ 11203 Series Advanced Ultrasonic Cleaner (Fisher Scientific)) for 30 minutes. Next, the solution was centrifuged at 7000 rpm for 5 minutes, and the supernatant was removed via vacuum line. An additional 10mL of cyclohexane was added and sonicated again for 30 minutes followed by centrifugation and supernatant removal. This process was then repeated twice with chloroform and anhydrous ethanol, followed by drying the particles in a vacuum desiccator.

3.3 Particle Characterization – Wettability

Contact angle measurements were conducted on silanized microscope slides, treated alongside colloidal particles using the silanization process described above following the procedure in the literature[75]. A water droplet was placed onto the treated slide and the contact angle was determined via the detection software provided alongside the tensiometer (Theta Lite, Biolin Scientific, Attension). Alternatively, monolayers were created via convective assembly technique by dispersing the particles (either colloidal or fumed particles) in ethanol and spreading the dispersion over a glass slide using a syringe pump. A dispersion of 5wt% and 3wt% fumed particles were used for TS – 610 particles and TS – 622 particles, respectively, and 30wt% for the treated colloidal particles as these concentrations resulted in close – packed monolayers. These monolayers were then used like the treated slides above to determine the water droplet contact angle on them.

3.4 Particle Characterization – size and charge

A 5ml aqueous dispersion of particles were prepared via dilution to 0.005wt.% by adding 100µL of ethanol to 0.25mg of particles held in a 20mL vial and stirred, followed by the addition of 5mL of DI water. The solution was then sonicated for 30 minutes until all particles are dispersed and no aggregates could be visually seen. Afterwards, the sample was left for 1 ½ hours to allow for ethanol evaporation, and water was added to fill to 5mL if necessary. The dispersion was then loaded into a 4.5mL cuvette and placed within the NanoBrook Omni Dynamic Light Scattering instrument (DLS, Brookhaven Instruments) to measure both the hydrodynamic radius and the zeta potential of the particles.

3.5 Foam Generation

Aqueous dispersions of fumed and colloidal particles at different concentrations, used in the generation of foam samples, were prepared by the following procedure. For fumed particle, 500 – 2000mg of particles were placed into a 50mL beaker. Next, 2mL of ethanol was added to the particles and stirred with a glass stir rod followed by the addition of DI water to bring the volume up to 50mL. After sonicating the solution for 45 minutes, the sample was left in the fume hood overnight to allow for ethanol evaporation. The absence of alcohol was checked by measuring the surface tension of the supernatant by drop shape imaging via Tensiometer. A similar procedure was conducted for the colloidal particles: 6wt.% (3g) of hydrophobically modified colloidal particles were added to a 50mL beaker, followed by 2mL of ethanol. The particles were mixed in ethanol briefly, and then 10mL of DI water was added. This solution was then sonicated for 45 minutes, and then 10mL more of DI water was added and sonicated for another 45 minutes. This process, with stepwise addition of DI water 10mL at a time, was repeated until the sample was fully dispersed and 50mL in total. All weight measurements were conducted via the Balance XS205DU (Mettler Toledo).

Foam generation was conducted via the Dynamic Foam Analyzer 100 (Krüss Scientific) (DFA100). The instrument has both air sparging and stirring methods, which can be utilized in generating the foam. All the foams analyzed in this study were prepared by sparging. To set up the prism column, which held the particle dispersion and the resulting foam, a sealing ring was inserted on the bottom of the cylinder, followed by a filter plate, and then by either a secondary sealing ring or an alternate sealing ring with slots for the liquid content probes. The filter plate used had pore sizes of 16 – 40µm. The prepared particle dispersion was added into the prism column of the DFA100 and sparged using .2L/min air flow rate to generate Pickering foams.

3.6 Foam Characterization

The DFA100 is equipped with a foam structure module; a camera, that utilizes the prism attachment of the column to generate images of the foam microstructure. The camera can be situated at various heights along the 250mm tall column, and at three separate positions away from the column which allowed for imaging at different magnifications ranging from 285 mm^2 (78.3px/mm), 140 mm^2 (112.3px/mm), or 85 mm^2 (145.6px/mm) mean field of view. For all experiments, the camera was situated at position 1 (285 mm^2), and at 75mm column height, with the midpoint of the camera at 68mm. The DFA100 is also equipped with a liquid content module (LCM) that could measure the resistance across the foam. The presence of 8 sensors placed along the height of the column allowed for the determination of the liquid content in the foam as a function of the foam height. The reference sensor, or the sensor that remained in the liquid phase through the entirety of the experiment, is 28mm above the filter plate, followed by sensors 1 – 7 being placed at 48, 68, 88, 108, 128, 148, and 168 mm, respectively. The liquid content probes were inserted into the column after the particle dispersion was added and before sparging took place. The LCM was then locked into place via a capping ring where it was then connected to the DFA100.

Figure 3.1. Frontal view of the Dynamic Foam Analyzer 100 (DFA100) (left); Liquid content module with electrodes (right).

3.7 Drop shape Tensiometry

The dilational behavior of particle – laden interfaces was probed using a tensiometer (Theta Lite, Biolin Scientific, Attension).

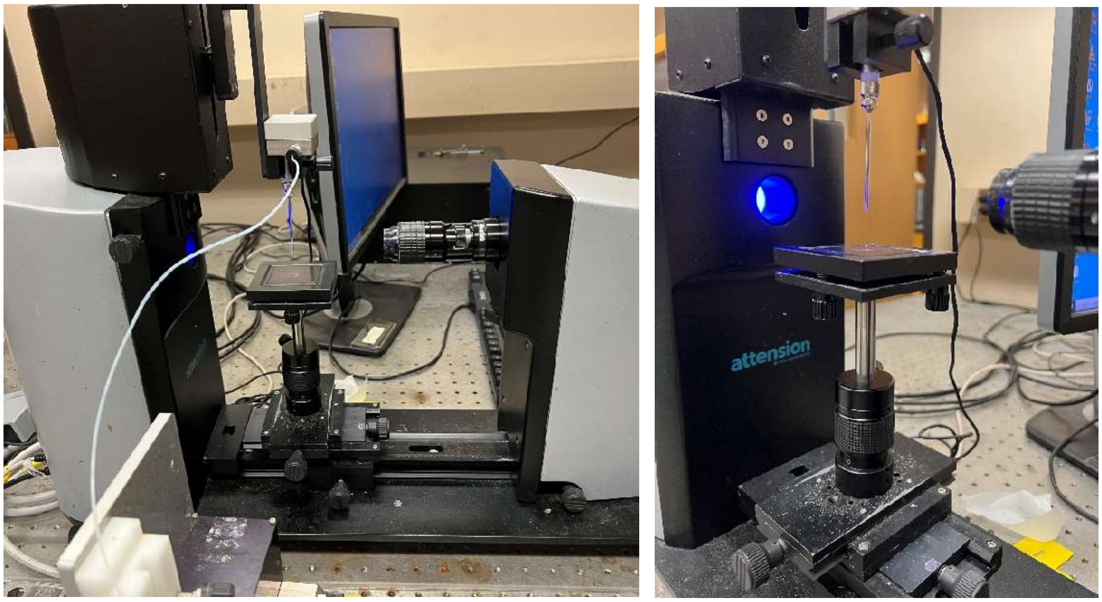

Figure 3.2. Drop shape Tensiometer setup (left) and the needle used for pendant drop experiments (right).

Pendant droplets of water were formed at the tip of a needle, either 10 or 14 gauge, onto which a secondary droplet containing the particle solution was added via a 50μL gastight Hamilton syringe. The particle dispersions were prepared in ethanol at concentrations of 1.5mg in 100μL (1.5mg/100μL) for fumed particles and 3.75mg/100μL for colloidal particles. Two needles of different gauges were utilized; a small, 14 – gauge, and large, 10 – gauge, needle with outer diameter sizes of 2.109 mm and 3.404 mm, which allowed for generation of droplets with a maximum volume of 37.5μL and 63μL, respectively. To generate the pendant droplets, DI water was run through the line to the needle, roughly 150μL, and then dispensed slowly to form the drop. To confirm that the system was without contaminant from previous trials, the surface tension was measured for the DI water droplet over a compression cycle. If the surface tension remained

~72.8mN/m during the entire compression, then deposition of the sample was conducted. Reduction of surface tension as a result of the droplet compression indicates that contamination was present in the sample, in which case, the needle was removed and cleaned with 2mL of ethanol followed by excess amounts of DI water. For the small needle, a 4µL pendant droplet was formed at the tip of the needle to which a 4µL secondary droplet containing the particle dispersion is added. The volume of the pendant droplet was then further increased to 20µL and left undisturbed for 15 minutes to allow for ethanol evaporation, after which dilatational experiments were performed. The procedure is identical for the large needle; the initial volume of the pendant droplet was 5µL in this case onto which 5µL of particle dispersion was added followed by increasing the volume of the pendant drop to 45µL to allow for evaporation. For oscillatory measurements, the droplet volume was decreased from its initial value, i.e., 20µL for the 14 – gauge needle, until specific surface tensions such as 70, 65, and 60 mN/m were reached. Once the surface tension was reached, the drop was then oscillated at 1Hz for 6 cycles followed by 0.1 Hz, with a maximum volume change of 0.2µL during pulsation which resulted in 1.41 – 3.85% total change in surface area during compression with an average of 2.42 ± .64%. After the trial has finished, the drop was compressed further decreasing the surface tension to the next value. This process was repeated until the collapse of the monolayer at which point the droplet shape could not be properly identified by the software.

3.8 Langmuir Trough Measurements

A custom – designed Langmuir trough (medium trough with inverted microscope window, Nanoscience instruments) equipped with a microscopy window is integrated with an inverted optical microscope (Olympus IX73 Research Inverted Microscope) to investigate the response and accompanying microstructural changes of particle – laden interfaces to compressions, shown below in Fig. 3.3.

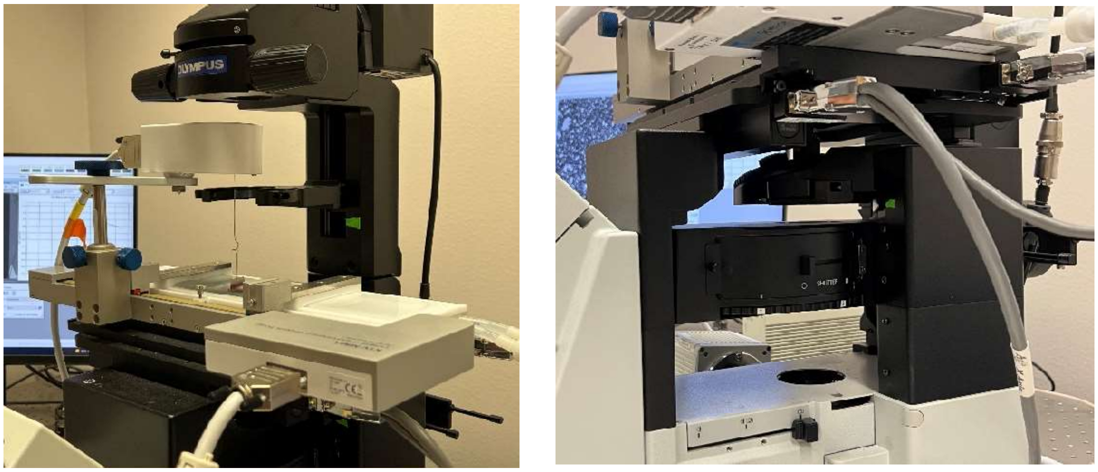

Figure 3.3. Langmuir trough (left) alongside the inverted microscope (right).

A platinum Wilhelmy plate was utilized to measure the change in the surface pressure as a function of the applied compressions. 100 µL of a solution of fumed (0.75mg/100µL) or colloidal (3.75mg/100µL) particles dispersed in ethanol was deposited on the interface in a drop – by – drop manner using a 50µL 1705N Hamilton syringe ; the trapped particles were spread on the surface via Marangoni flows. A wait period of 30 minutes was allocated to allow for the evaporation of the spreading solvent. The total area of the open and closed states were 180cm^2 and 25cm^2 respectively. Compressions were conducted at a rate of 15 cm^2/min.

3.9 Shear Rheology Experiments

The double wall ring (DWR) accessory in a TA – DHR2 stress – controlled rheometer was used to perform shear rheological measurements on particle – laden interfaces. In order to examine the shear response of monolayers at different area fraction of particles at the interface, corresponding to different surface pressures, a ribbon trough (nanoscience Instruments, Langmuir Ribbon Barrier Trough) was integrated with a custom – designed double – walled ring (DWR) as previously done by Vermant and coworkers[85].

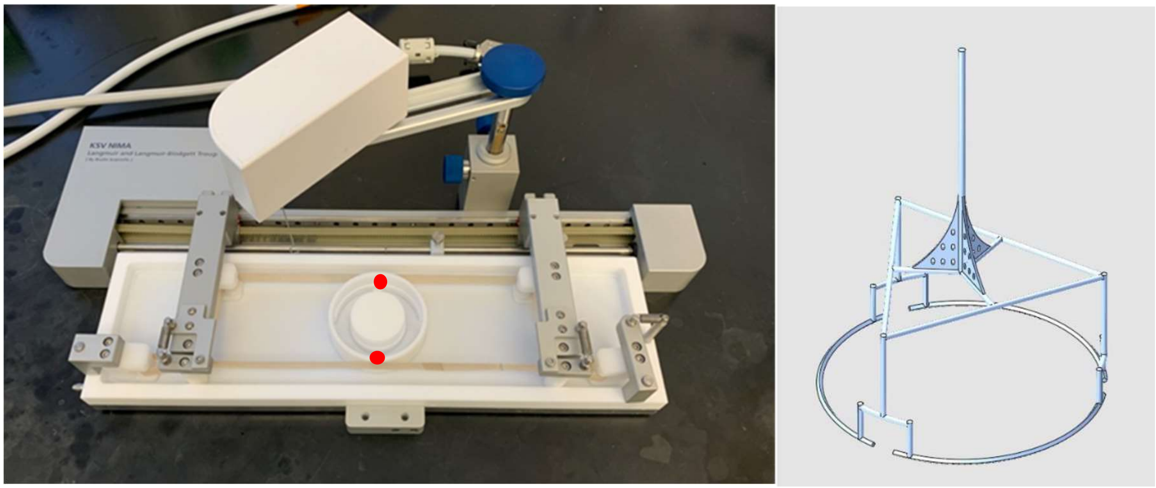

Figure 3.4. Ribbon trough with DWR setup (left). Red circles indicate where the particle deposition was carried out. Diagram of the DWR (right).

The cup was placed inside the trough first, followed by addition of DI – water as the subphase. 100 μL of a solution of fumed (1.5mg/100μL) or colloidal (7.5mg/100μL) particles dispersed in ethanol were deposited inside the ring, at two locations in between the cup openings and at opposite sides of the ring indicated via red dots in Fig. 3.4. After 30 mins had passed (to ensure the evaporation of the spreading solvent), the ring was lowered towards the interface. Positioning of the ring at the interface was carried out by tracking the magnitude of the axial force and then lowering the ring 500μm to its halfway point once force was measured by the rheometer. Use of compression via ribbon trough alongside the DWR geometry allows for shear experiments at specific surface pressures. The experiments conducted were amplitude and frequency sweeps at surface pressures ranging from open state to 50mN/m. The amplitude sweeps were conducted at 1 Hz, over a range of strains 0.001% – 100%. The frequency sweeps were conducted within the linear viscoelastic regime at 0.05% strain, over a frequency range of .001 Hz to 100 Hz. The total area of the open and closed states were 150cm^2 and 60cm^2 respectively. The compression was done at a rate of 15 cm^2/min.

3.10 Particle Characterization – Microscopy

A small piece of silicon wafer, 0.5 · 1 cm^2, was placed onto a support on the bottom of the Langmuir trough, such that the height of the surface of the silicon wafer was above the bottom of the barriers as shown below in Fig. 3.5. Because the bulk liquid was vacuumed from above, if the wafer was not above the bottom of the barriers, the vacuum would disturb the monolayer before a successful deposition could take place.

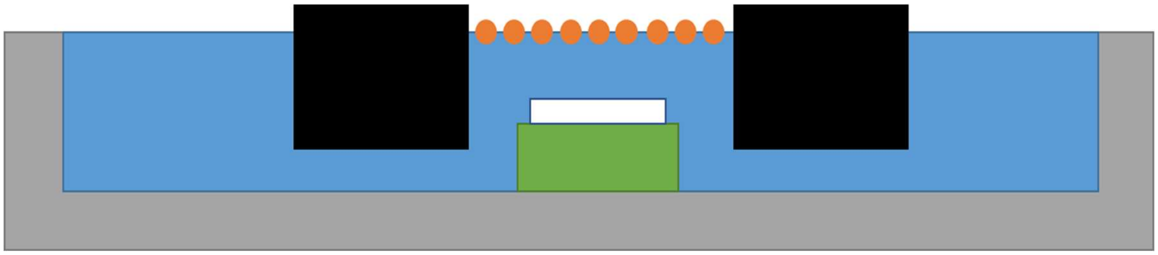

Figure 3.5. Schematic of particle monolayer deposition onto a silicon wafer.

The grey represents the Langmuir trough, blue indicates the DI water subphase, and the black squares represent the barriers that can open (move towards the trough walls) or compress towards the middle. In the center, the silicon wafer (white) was placed onto the support (green) such that a particle monolayer (orange) can be deposited onto the wafer during subphase removal via aspiration through a vacuum line. The deposition process started with the trough being filled with water followed by particle solution deposition onto the interface via 50μL 1705N Hamilton syringe, 0.5mg/100μL for TS – 622 fumed particles and 1.875mg/100μL for colloidal particles, respectively. A period of 30 minutes was allowed for the evaporation of the spreading solvent. Next, water was aspirated from the sides of the trough outside of the barriers to ensure the monolayer of particles was left undisturbed. Aspiration was continued until the water level was below that of the silicon wafer in order to deposit a particle monolayer onto the silicon wafer. The wafers were then removed via tweezers and placed in a vacuum desiccator to dry overnight. For Atomic Force Microscopy (AFM) (Park NX10, Park Systems), the only addendum was that the silicon wafer had tape placed over half of the surface so that after drying the tape could be removed allowing for analysis of the height of particle monolayer, easily distinguishable from the bare wafer using a tip of size 5nm. For Scanning Electron Microscope (SEM), a sputter coating of iridium was used to reduce charging effects of the particles before placing them in the SEM (NEON Field – Emission Scanning Electron Microscope, Zeiss) which utilized a voltage of 5kV.

3.11 Image Analysis

When capturing images of the particle monolayers, objective lenses of 10x (numerical aperture (NA) = 0.25, working distance (W.D.) = 10.5mm) , 20x (NA = 0.45, W.D. = 6.6 – 7.8mm), and 60x(NA = 0.7, W.D. = 1.5 – 2.2mm) were used for imaging. 100 μL of a dilute solution of fumed (0.3mg/100μL) or colloidal (1.5mg/100μL) particles was utilized to obtain a low surface pressure at the interface initially. The trough was also closed to 150mm^2 for an initial starting area to mimic the area of the ribbon trough. One drop of the particle solution was added initially to adjust the position of the objective and find the interfacial plane containing the particles. An empty location was created in front of the objective via small solution deposition such that an image could be taken so that the background could be subtracted by the software (HC Image Live). After this, the rest of the particles were added, and a wait period of 30 minutes was necessary. Next, compressions were conducted to reach certain surface pressures (5mN/m, 15mN/m, etc.) and the interface was imaged. 6 images were recorded using the 10x objective at 14 separate surface pressures, i.e., 4, 11, 15mN/m etc., and 40 images using the 10x were recorded at more widespread values of 4, 11, and 23 mN/m.

Images captured by the Olympus IX73 Research Inverted Microscope were analyzed using various methodologies in attempts to obtain the best binary representation of the base image. The first method shown below was using ImageJ and manually thresholding the image, until the processed image matched the original. This method worked well for the colloidal particles but faltered once packing started to approach a maximum. The second method in ImageJ, shown in Fig. 3.6, was more involved and proceeded as follows: First, Gaussian Blur with a sigma value of 2 was applied to the image. The image was then altered via Enhance Contrast, with 3% saturated pixels, and both the Normalize and Equalize Histogram settings enabled. Then ‘Find Edges’ was utilized to differentiate between the background and the particles, followed by Sharpening and the math processing Multiply by 2 pixels. Lastly, the image was made binary. This method worked reasonably well for most images, such as low or high coverages.

Figure 3.6. Image analysis of a colloidal interfacial monolayer during compression. a) Base image without corrections; b) Image after manually thresholding; c) Image after Gaussian blur, Enhance Contrast, and Find Edges performed; d) Image C after Sharpening, Multiply, and Make Binary were performed.

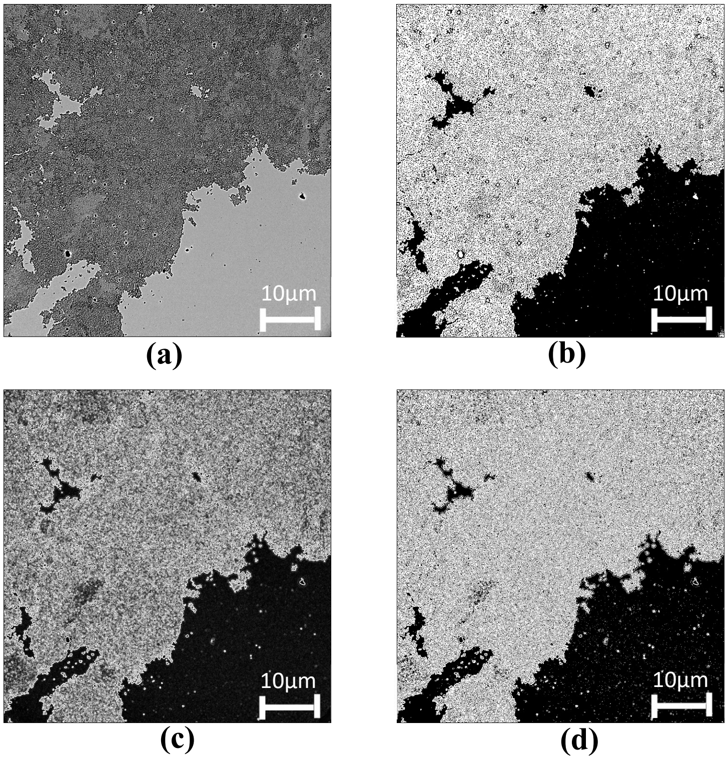

The last method was used for images that had low coverage of particles in ImageJ: Gaussian Blur with a sigma value of 2 was applied to the image, followed by background subtraction of 50 pixels. Enhance contrast with 30% saturated pixels was then used, followed by Find Edges, and lastly made binary. The latter two methodologies were useful during batch processing; however, the accuracy of the manual thresholding was found to be higher overall and was used the majority of the time. After the images were converted to binary, the Analyze Particles selection was used to calculate the total coverage of particles in the images which was that averaged at each surface pressure. For fractal analysis of the images after they were made binary, the FracLac plugin[86] was utilized with the following settings: 12 grids, 7 sizes of boxes with a minimum size of 7 and maximum of 2%, open raw data in Files, with no graphic options on. This allowed for the least number of windows to open while still being able to obtain the fractal dimensions as well as coverage values from FracLac to compare to the ImageJ values.

3.12 Viscosity Measurements

Measurements were performed using the 40mm cone (2º incline) with plate accessory of the TA – DHR2 stress – controlled rheometer, as well as with the bob and cup accessory for lower viscosity fluids. Before adding the particle solution, the accessory and rheometer were calibrated to ensure accurate readings such as rotational mapping and torque. When using the cone and plate, 610µL of particle solution was pipetted onto the plate directly below the cone accessory, such that when the cone was lowered to 58µm the solution would spread to contact all areas of the cone. Once the cone was lowered, excess solution was sponged using Kim wipes (Kimtech) and then the cone was further lowered until the tip was 53µm above the plate. The solution was then sheared from 0.02 – 119.4s $^{-1}$ to gather the viscosity data. Calibration was done for the bob and cup accessory before use as well, and 23mL of particle solution was added into the cup before the bob was lowered to the geometry gap of 5900µm. After lowering the bob, viscosity trials were performed for shear rate values in the range of 0.02 – 119.4s $^{-1}$.

4. Particle and Solution Characterization

4.1 Wettability

Advancing contact angle measurements for the fumed particles were performed on slides that had particle monolayers deposited onto, while the colloidal particle's advancing contact angles were obtained via particle monolayers and slides that had undergone the same treatment methodology as the colloidal particles themselves. The two fumed particles, LSA and MSA, were found to have contact angles of around 135.2 ± 14.1° and 140.2 ± 2.5° respectively, while the colloidal contact angles were measured to be 125.9 ± 10.6° and 87.3 ± 7.2°, for the particle monolayer slides and DMDCS treatment respectively. This discrepancy in the colloidal contact angles was the result of added roughness when particles are deposited onto the slide compared to just the silane groups which can increase the hydrophobicity of the surface. Both fumed particles were more hydrophobic than the treated colloidal particle in part to their larger surface area which allowed for more DMDCS groups to be attached, as well as the impact of the particle roughness on the pinning of the contact line. All particles have some degree of roughness causing imperfections on the surface which the contact line follows to reduce the overall interfacial energy. The fumed particles not only have this roughness associated with preparation but are also amorphous due to their chain – line structure, which can lead to more surface undulations that would pin the contact line.[87-89]

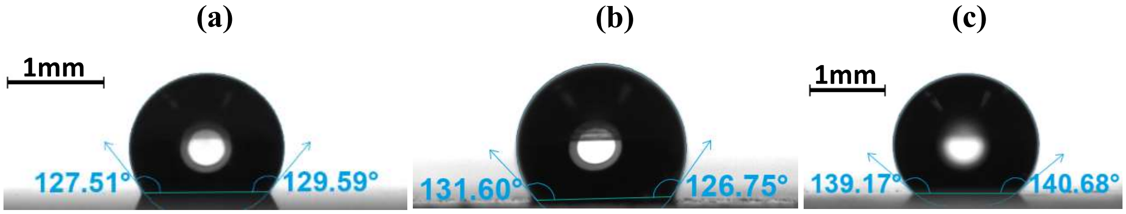

Figure 4.1. Contact angle measurements carried out using a water droplet deposited onto a monolayer of (a) colloidal, (b) LSA, (c) MSA particles on a glass substrate.

4.2 DLS & Zeta Potential

DLS and zeta potential measurements were conducted to determine the hydrodynamic radii of the particles in solutions as well as to examine the charges of the particles. For the zeta potential measurements, it was determined that the LSA and MSA were both negatively charged with values of -22.79 ± 2.38mV and -25.83 ± 0.99mV. Untreated colloidal particles had a zeta potential of -52.02 ± 2.02mV while the colloidal particles treated with DMDCS had a zeta potential of -30.54 ± 2.01mV, meaning that the treated colloidal particle has more charged groups leftover after silanization than both the fumed particles used. All of the particles had moderately negative zeta potentials which indicated that these particles should be relatively stable in solutions, however as discussed later the modified colloidal particles were unstable in the solution compared to their fumed counterparts.

With regards to the hydrodynamic diameter measurements of the particles in solution, there were some discrepancies caused by suspected particle aggregation within the solution leading to a bimodal size range for all particles tested. As shown in Fig. 4.2 for the MSA sample examined, there are two main peaks that can be seen around 150 –

250nm and 900 – 1000nm. This phenomenon can be seen for both the LSA and the colloidal particle samples that were tested. If all the peaks were considered, the hydrodynamic diameters of the particles would be 355.6 ± 4.93nm, 344.66 ± 21.57nm and 833.97 ± 712.6nm for the colloidal, LSA, and MSA respectively. In order to elucidate the actual size of these particles, we utilized scanning electron microscopy (SEM) to measure individual particles, discussed in the following paragraph, and compared the values to what is shown on the intensity graphs. Based on the SEM data, the most likely peaks for all of the particles were the lower peaks between 150 – 300nm and so those data sets were utilized to garner the average hydrodynamic diameters, while the large peak was taken as aggregation and was not included in the averages. The corrected averages then for the particle hydrodynamic diameters were 322.3 ± 120.9nm, 189.37 ± 15.71nm, and 196.51 ±

70.11nm for the colloidal, LSA, and MSA respectively and are the sizes that will be used from this point onward.

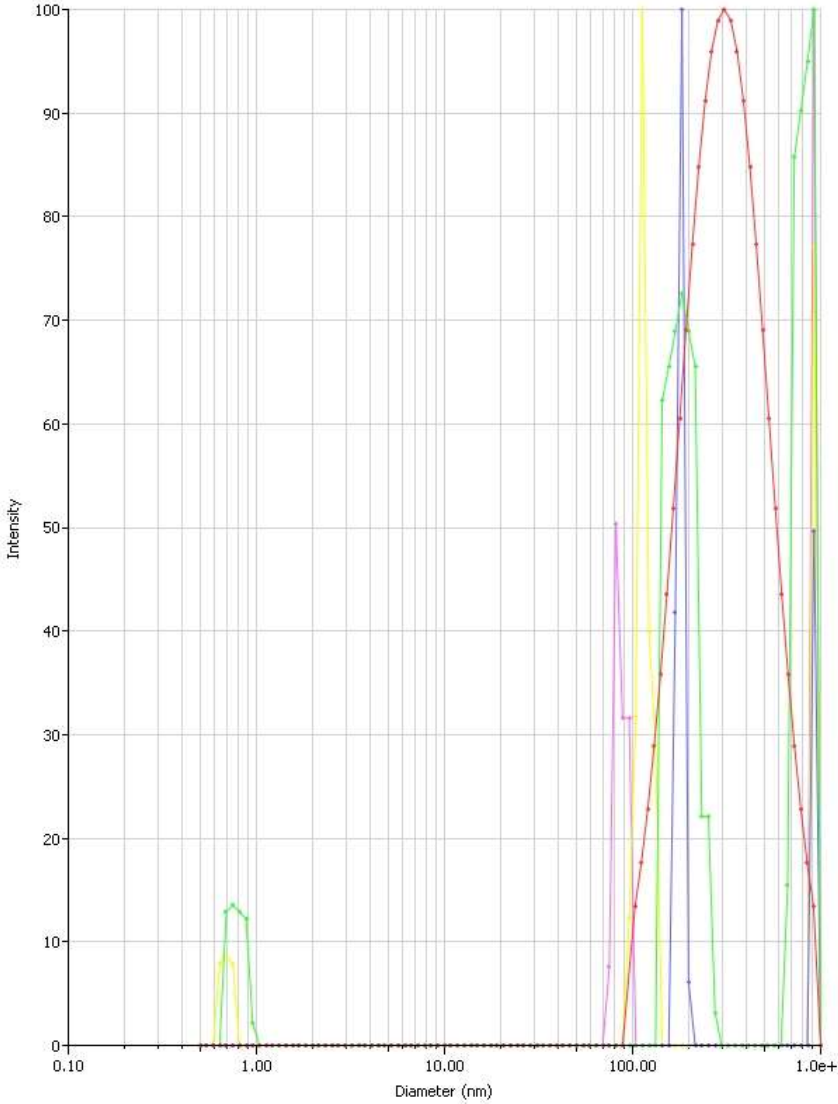

Figure 4.2. An example of DLS Intensity graphs obtained for MSA particles.

4.3 SEM & AFM

To conduct SEM and atomic force microscopy (AFM), a monolayer of particles placed onto the air – water interface was deposited onto a silica wafer as discussed above and dried in a vacuum desiccator overnight. The wafer used for AFM measurements had tape on one side; the tape was removed after the step and served as a baseline for measuring the height of the particle layer. For SEM, the wafer was coated with iridium so that the effects of charging of the wafer and monolayer was mitigated before use. Shown in Fig. 4.3 & Fig. 4.4 are images taken of both the MSA and colloidal monolayers that were deposited onto the silica wafer. From these images, it can be clearly seen that the colloidal particles do not have diameters exceeding 300nm, with an average diameter of 283 ± 28nm; this information was used to pick the most accurate peaks in the DLS as discussed in previous section. As the fumed particles are constructed via fused 20nm base silica particles, the diameter of the fumed particles was much more difficult to analyze. Therefore, the wafers containing half particle monolayer and half empty space were examined using AFM to characterize the height of the monolayer to determine how they compared to the estimated hydrodynamic diameter to better grasp the particle sizes.

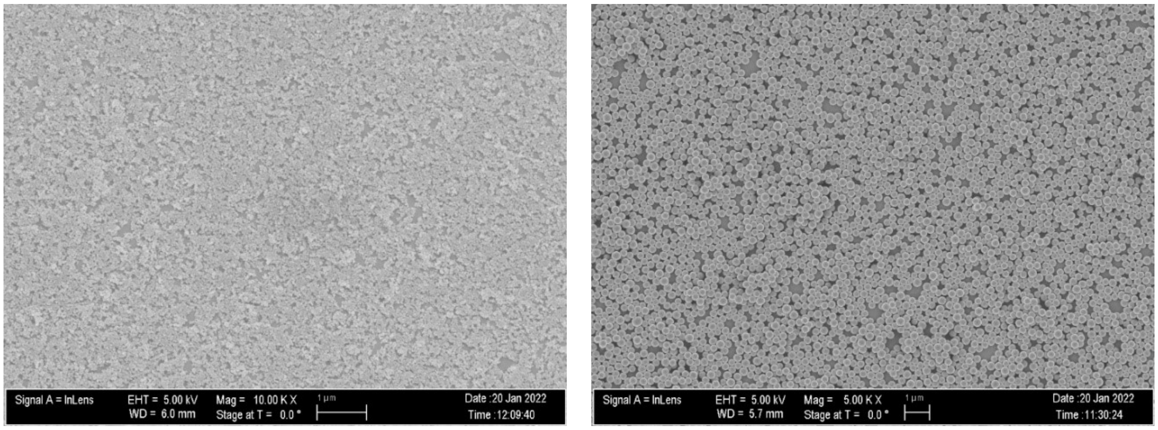

Figure 4.3. SEM images of MSA (left) and DMDCS treated colloidal particles (right).

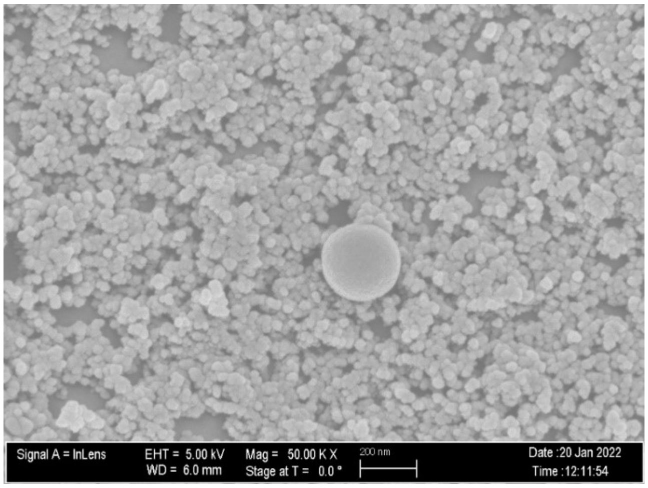

Figure 4.4. MSA & colloidal particles side by side comparison.

AFM was conducted onto half – taped wafers such that a clear separation was made between the particle monolayer and the bare silicon wafer. Shown in Fig. 4.5 & Fig. 4.6 are images obtained for both the fumed and colloidal monolayers, as well as the color scale representing the total height measured with regard to the base line. These images were taken at the edge of the particle monolayer, such that bare silicon wafer spots could be used as a baseline to indicate the overall height of the formed monolayer of particles. As the heights shown via the color indicator are relative, the overall change in height, such as ~250nm from – 150nm to 100nm, must be used to quantitively address the height of the particle monolayer. With regards to the colloidal images, it can be clearly seen that average peaks for the monolayers reach upwards of 250nm, which is within the standard deviation of diameter size seen by the SEM as well as similar to the hydrodynamic diameter found via DLS measurements of 322.3 ± 120.9nm. For the fumed, which had a hydrodynamic diameter of 196.51 ± 70.11nm, it can be seen that the maximum peak height value was around 200nm and with many values ranging from 40 – 100nm. This large discrepancy in difference between the hydrodynamic diameter and the average height of the particle monolayer shows that these particles could rearrange at the interface as they are amorphous instead of purely spherical due to the nature of the fused silica chains. This expansion at the interface leads to interesting and diverse interfacial properties compared to the hard–spherical colloidal particles and is discussed in more depth in later sections.

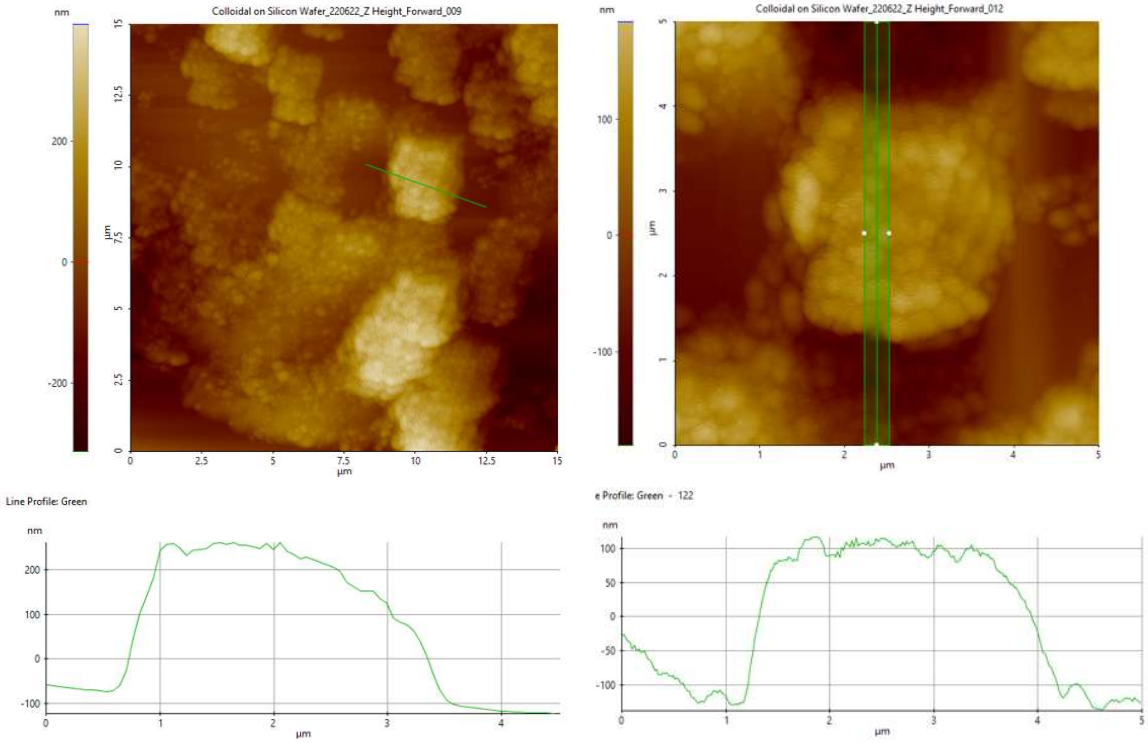

Figure 4.5. AFM images for colloidal particles (top) along with height graphs of the respective image (bottom).

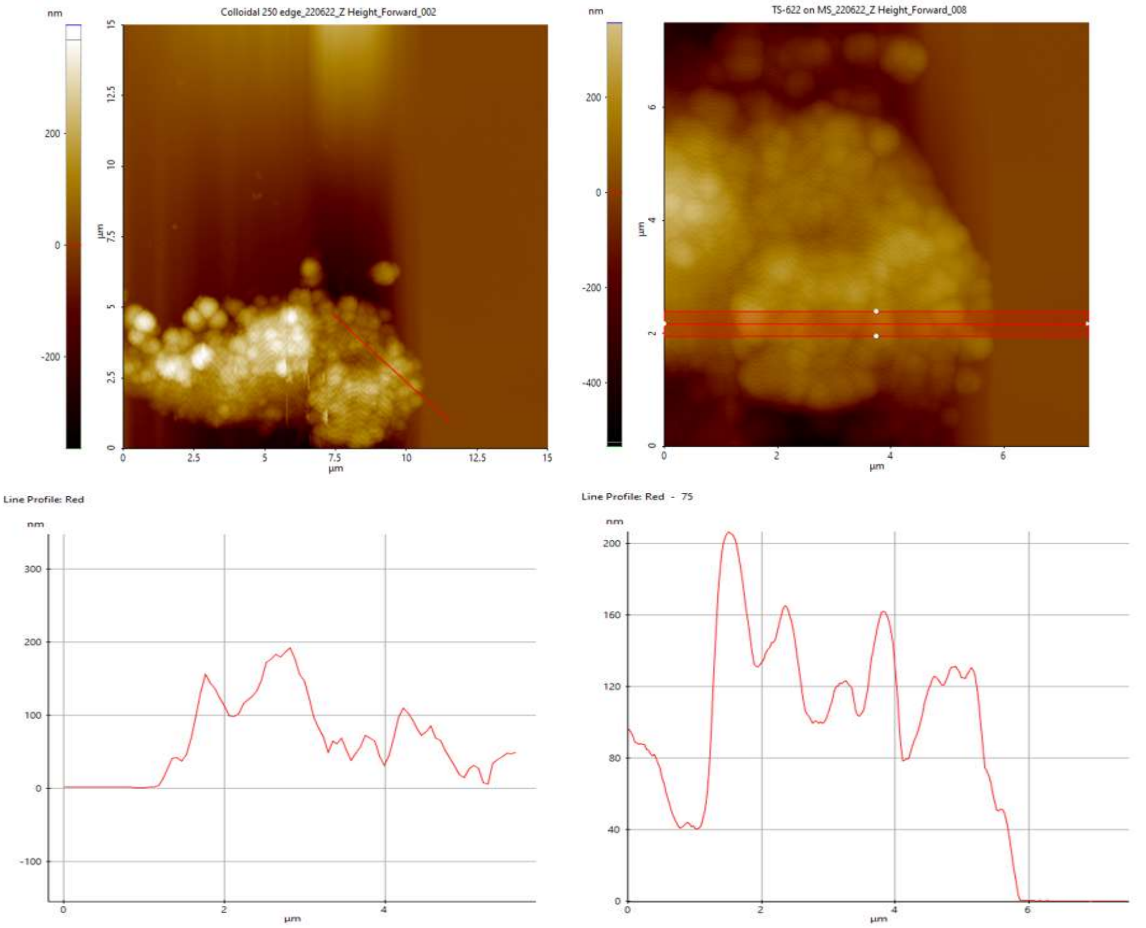
Colloidal 250 edge_220622_Z Height_Forward_002

TS-622 on MS_220622_Z Height_Forward_008

Line Profile: Red

Line Profile: Red - 75

Figure 4.6. AFM images for MSA particles (top) along with height graphs of the respective measured area (bottom).

4.4 Bulk Solution Viscosity

Bulk viscosity was tested on each particle solution, at varied concentrations, to connect the solution characteristics to the resulting foam characteristics and properties. In order to accurately measure the viscosities, as the solutions tended to have low viscosities, the cone and plate as well as the bob and cup geometry were utilized. Shown below in Fig. 4.7, comparing the geometry used, it can be seen that the values for viscosity with shear rate are near identical between the two geometries for the fumed solutions, which were the lower viscosity solutions. Because of this, the cone & plate geometry was utilized to conduct the wider range of concentrations as well as for the colloidal samples shown in Fig

4.8. With regards to the particle samples themselves, both samples show shear thinning behavior and both have increasing viscosity with increasing particle concentration in the aqueous solution. The fumed samples have initial values of 83 ± 56cp for 0.5wt.% to 1,100 ± 440cp for 2.0wt.% at 0.1 1/s, while the colloidal sample had higher viscosity measurements of 5,340 ± 1,260cp for 3.0wt.% to 12,772 ± 1,051cp for 6.0wt.% at 0.1 1/s. It has been shown that increased viscosity has negative effects on the resulting foam generation, namely the foamability of the solution, as more energy is required to adequately mix the air and solution to form the foam. [47] As will be shown later, the overall foamability of the solutions were not different most likely due to the limited time that the solutions were sparged. If the solutions had been sparged continuously until the foam height no longer changed, i.e., the maximum total foam height that the solution could produce, then there could be variance in the foamability. Furthermore, increased viscosity has been shown to increase the stability of the resulting foam, as well as its ability to resist destabilization.[37, 42, 47, 61] Based on these observations, the colloidal foams should better resist destabilization than the fumed foams due to its larger viscosities with concentration, and this will be explored in the following section.

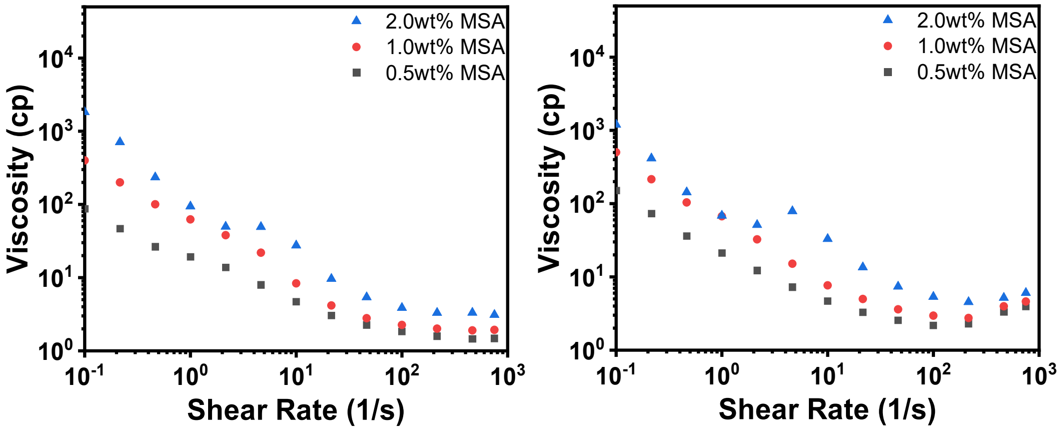

Figure 4.7. Comparison of Cone & Plate method (left) and the Bob & Cup method (right) for viscosity measurements carried out on MSA particle dispersions at various particle concentrations.

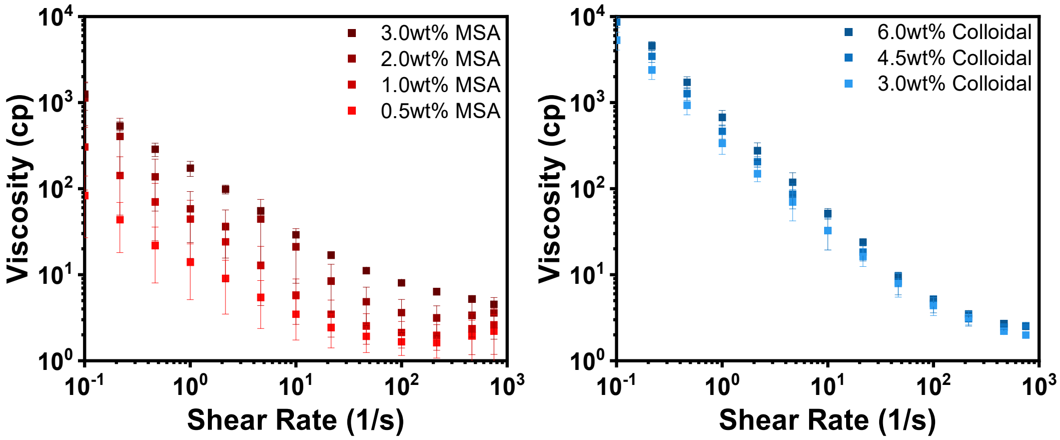

Figure 4.8. Viscosity trials of MSA fumed (left) and colloidal (right) particle dispersions via cone & plate methodology.

5. Foam Stability

5.1 Foam Height & Half–life

The first components that must be investigated are the foam properties, such as half–life and bubble characteristics, and how they are altered when particles are used to stabilize the bubbles compared to widely used foaming agents. Shown below in Fig. 5.1 is the total height of three trials consisting of fumed particles, colloidal particles, and SDS. The initial foam heights of all three trials are approximately the same at around 135mm, which indicated similar foamability within the short sparging time of 30s; however, there was a noticeable decrease in the surfactant – stabilized foam height throughout the hour. The particle samples maintained a relatively constant height, which highlighted their ability to resist destabilization unlike the surfactant over the same time span. This can be attributed to strong particle adsorption at the interface as well as strong interparticle interactions causing a well – linked network to form at the interface. The surfactant does not have as strong as a desorption energy required to be removed from the interface, which allows the molecules to migrate freely from the interface back into the bulk and vice versa based on the total area available to the molecules. Due to this, as well as not creating a network at the interface armoring the bubbles, the SDS foam was unable to resist destabilization to the same degree over the hour.

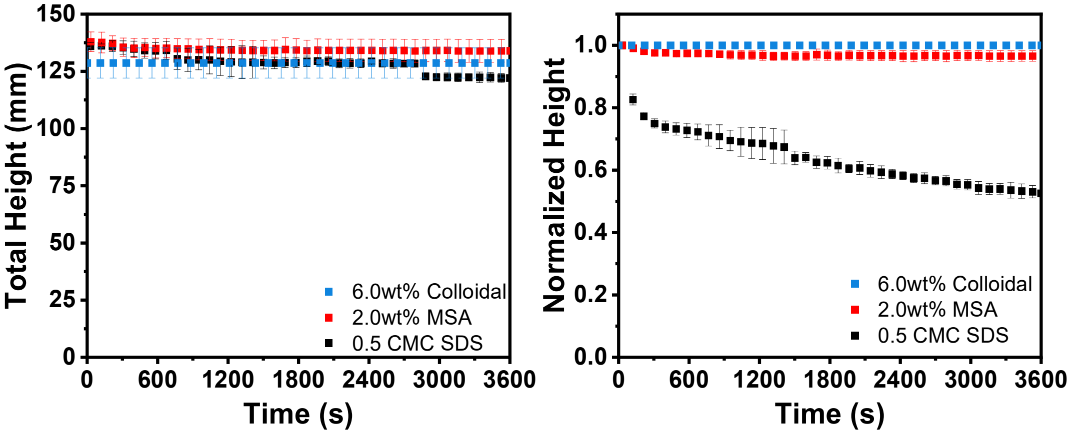

Figure 5.1. Total height (foam + solution) for systems stabilized with different stabilizing agents (left); Normalized height (H/H_0) for the same systems stabilized with different agents (right).

After establishing that particle – stabilized foams are more stable against coalescence and Ostwald ripening than a surfactant – stabilized foam, the effect of particle concentration on the foam height and half – life was investigated. Shown in Fig. 5.2, for the MSA fumed silica particles, an increase in the concentration had negligible impact on the height of the foam if the foaming parameters themselves, i.e., sparging time and initial solution volume, are held constant.

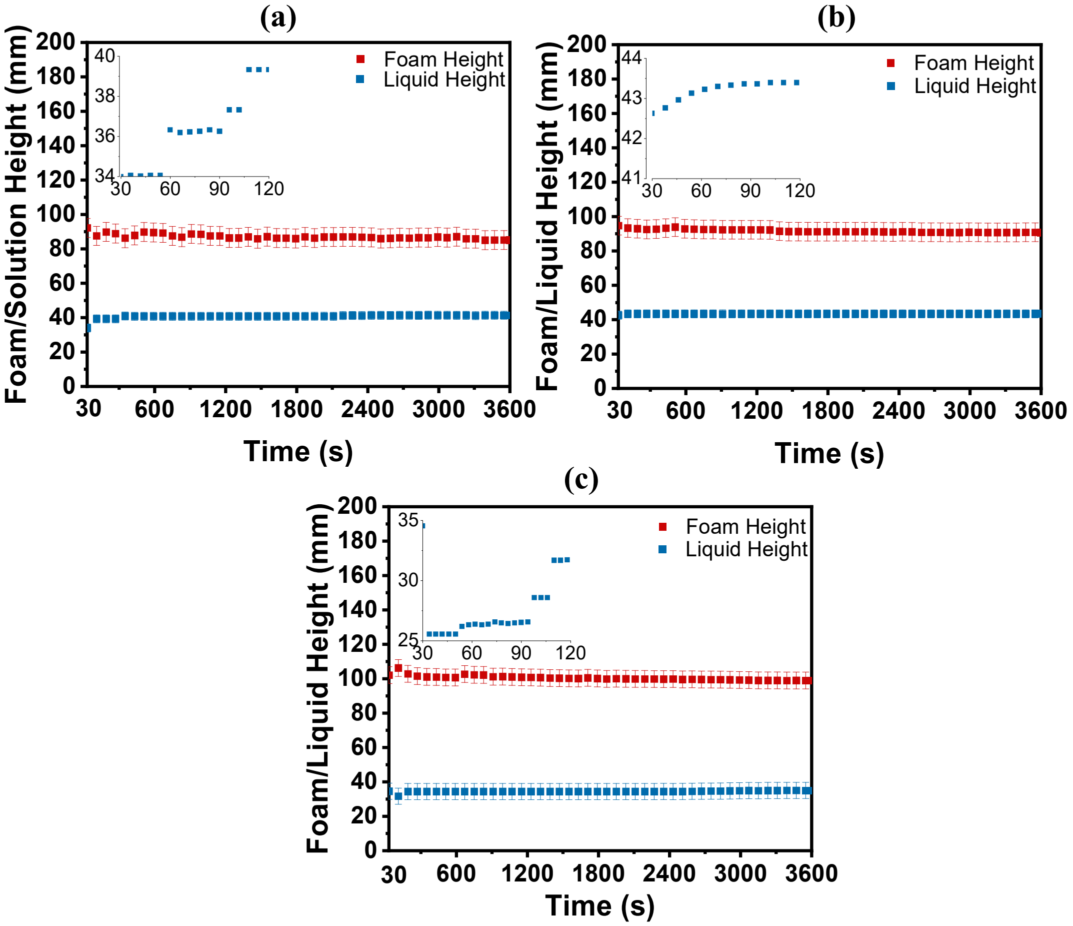

Figure 5.2. Foam height and drained liquid height as a function of MSA fumed silica particle concentrations of (a) 0.5wt%, (b) 1.0wt.%, and (c) 2.0wt.%; Inset is a closer look at the drained liquid height over a smaller timescale to highlight drainage over time.

Therefore, while there might be more opportunity for new bubbles to be stabilized by an increased number of particles, the concentration itself was not tied to foam height at small sparging times for these foams. However, when the foams were observed for longer than an hour to investigate their half – lives, an appreciable dependence on concentration was recorded. Shown in Fig. 5.3, when the concentration of the MSA foam was increased from 0.5wt.% to 2.0wt.% in the solution, the half – lives not only increased from 3.2 hours to 109 hours but appeared to follow a linear dependence on concentration.

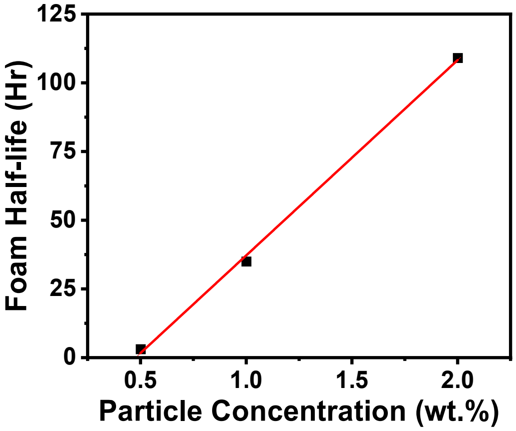

Figure 5.3. Foam half – life for MSA fumed silica particle – stabilized foams as a function of concentration.

While the amount of foam generated remained the same for both samples at around 100mm, increasing the number of particles provided a strong interfacial particle network and created an 'armor' around the bubbles, which allowed them to resist destabilization more effectively. Liquid drainage of the foam still occurred as shown by the insets in Fig. 5.2, which led to the foam drying out and eventually destabilizing; however, this process proceeded more slowly allowing for the long foam half – lives. It is expected that eventually the foam half – life will plateau at higher concentrations due to the overabundance of particles and an eventual lack of surface area for them to occupy. Trials were also attempted using .25 wt.% of the fumed silica particles, however these foams were unstable and would not survive past the initial foaming time. This lack of foam stability indicated that there was a minimum number of particles necessary to either partially or fully cover the surface of bubbles in the foam. If this minimum was not met, the foam was unstable. With regards to this concentration dependence, the foam qualities of each foam were calculated. The foam quality, $FQ = \frac{Total\ gas\ volume\ added}{Total\ foam\ volume} * 100$, was 77%, 73%, and

81% for 0.5 CMC SDS, 2.0wt% MSA, and 6.0wt% colloidal particles, respectively. Values above 60% have been shown to create stable foams in which the gas bubbles are polyhedral in shape and have thin lamellae.[90] This was seen by all the foams, even though the SDS foams were much more unstable overall compared to the particle foams. For fumed particle solutions at lower concentrations, the foam quality increased up to 89% for 0.5wt%. This suggested that as the concentration was lowered the foam quality would continue to increase up towards the maximum value determined for stable foams which is 97%. In most cases past 97%, the solution makes an aerosol and no longer can create foam. With regards to these Pickering foams, no visible aerosol was formed, so instead the particles could not create a network in which the gas could be trapped and thus the gas diffused through the solution. Comparing the fumed particles with the colloidal particles through Fig. 5.2 & Fig. 5.4, it can be seen that the foam heights and stability are very similar over the same time period, with the total height of 130mm for the case stabilized by fumed particles and the total height of 136mm for foams stabilized with colloidal particles, which remained stable for the entire hour. To fully investigate the minutia between fumed and colloidal particle impacts on foam stability we look toward the osmotic pressure of these systems shown in the next section.

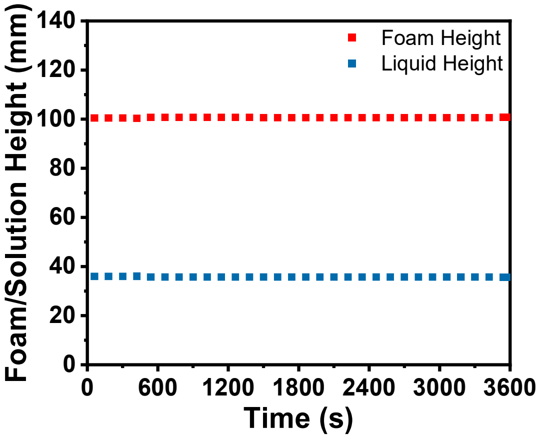

Figure 5.4. Foam height and liquid height for 6.0wt.% colloidal – particle stabilized foams over 3600s.

Solution preparation was very impactful on the resulting foaming capabilities and characteristics. Firstly, if not enough ethanol was used to fully coat the particles and was not mixed well into the particles initially, then some of the particles would not be wetted by water and would remain on the surface of the solution resulting in a lower concentration of particles in the solution than desired. However, care must be taken when introducing the fumed particles to ethanol as extended times in low ethanol volumes can lead to gelation.[91] Two separate methodologies were used before the finalized version was decided upon. The first was mixing the particles with 10 – 20mL of ethanol in a centrifuge tube, and then centrifuging the solution so that the ethanol could be removed via vacuum line. What occurs however was that in low ethanol volumes with high particle concentration the particles began to gel, which led to different foam characteristics and lack of particle dispersion in the aqueous solution. This was also observed when the fumed silica particles were immersed in 2 – 3mL of ethanol and left overnight. This led to the method of adding water after the initial ethanol addition, which increased the evaporation time for the ethanol which was no longer removed via centrifugation but enabled for more dispersion into the solution and no gelation of the particles.

Other methods of sparging and foam generation were also conducted such as sparging at higher air flow rates as well as stirring the solution. Air flow rates were tested from 0.2L/min to 1.0L/min, and it was seen that at higher flow rates a more polydisperse foam was generated than at the lower flow rates. This was likely due to the increased energy input into the system that potentially prevented the particles from evenly coating the bubbles during their formation, which led to a large array of sizes. When different filters were utilized with larger pore sizes, similar trends were seen with regards to the polydispersity with flow rate, and that the bubble sizes were overall larger due to the larger pores being used. Ultimately, the smallest pore size filter, 16 – 40μm, and lowest flow rate, 0.2 L/min, were selected to make a uniform foam that could be generated consistently and repeatedly. Stirring was attempted as well, although it was not characterized in much detail as the sparging system. Briefly, when the solutions were stirred they were able to make foams however at a much lesser degree in total volume, such that even at the lowest camera position the foam was only partially visible. The foam itself was very monodisperse and contained bubbles on the orders of magnitude smaller than that created via sparging. This is believed to be caused by the large amount of energy being added into the system by the stirrer, which was able to stir up to 8000rpm. Due to the inability to properly capture the stirred foams without increasing the solution size as well as the inability to use the liquid content modules with the stirring setup, the sparged foams were chosen as the focus of this thesis and were investigated to a greater depth in terms of their abilities to resist destabilization.

5.2 Osmotic Pressure

When a foam is generated, the bubbles are spherical and dispersed within the solution. After some time, t, the liquid will drain from the lamella and the bubbles themselves will come into contact and begin to lose sphericity and become more polyhedral in shape. The spherical shape is the minimum interfacial energy state, and so when the bubbles become polyhedral, and thus increase in energy, the system attempts to 'reform' the sphericity by flowing the continuous phase back into the bubbles. Osmotic pressure, Π, is the pressure within the bubbles that resists the flow of water inwards and maintains the polyhedral shape. Fig. 5.5 illustrates the development of osmotic pressure within a liquid foam system, and highlights that as the bubbles become more polyhedral the osmotic pressure will increase to counteract the infiltration of the continuous phase. And because the bubbles become more polyhedral as the lamella drains around them forcing the bubbles into closer contact, osmotic pressure can be directly tied to the liquid drainage of the system.

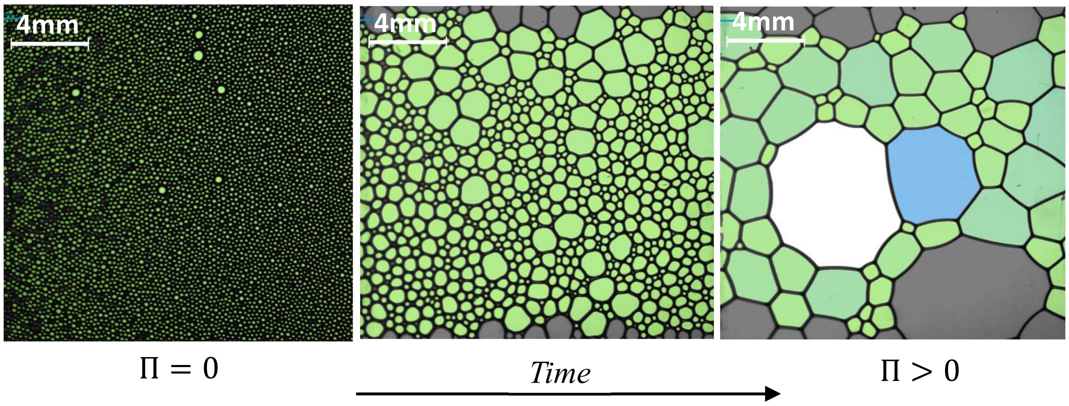

Figure 5.5. Change in the osmotic pressure with time for foams generated from 0.5 CMC SDS solutions.

From the osmotic pressure of the system, we can investigate the liquid drainage, one of the destabilization mechanisms, in the particle – stabilized foams produced. To obtain values for osmotic pressure, we make use of the liquid content attachment of the DFA100, which measure the resistances across foam that lies between two sensors. The equation used to associate the conductivity, which is the inverse of resistance, with the volume fraction of the continuous phase, water, is shown below: [92]

$$\varepsilon = \frac{3\sigma(1+11\sigma)}{1+25\sigma+10\sigma^2} \qquad (2)$$

Were σ is relative conductivity $\sigma_{\text{sample}}/\sigma_{\text{liquid}}$ and ε is the volume fraction of the continuous phase. Σ_{sample} is the conductivity being measured at each sensor location 1 – 7 along the column, while σ_{liquid} is the conductivity of the reference sensor that remained within the liquid solution after sparging. E can then be associated with the osmotic pressure of the system by: [70]

$$\Pi = K\frac{\gamma}{R_{32}}\frac{(\varepsilon_c - \varepsilon)^2}{\sqrt{\varepsilon}} \qquad (3)$$

Π is the osmotic pressure, γ is interfacial tension (mN/m), R_{32} is the Sauter mean radius of the bubbles (m), and ε_c is the critical volume fraction of the system of either 0.26 or 0.36 depending on whether the system is mono – or polydisperse, respectively. K is a constant associated with the polydispersity, being either 7.3 or 3.2 for mono – or polydisperse foams, respectively.[93, 94] By dividing by γ/R_{32}, the reduced osmotic pressure $\overline{\Pi}$ can be calculated, which allows for comparison between different systems. From the equation it can be seen that $\overline{\Pi}$ is inversely proportional to ε, so as the volume fraction of the continuous phase present in the lamellae decreases, the reduced osmotic pressure will increase which validates the use of $\overline{\Pi}$ as a tool to investigate liquid drainage over time.

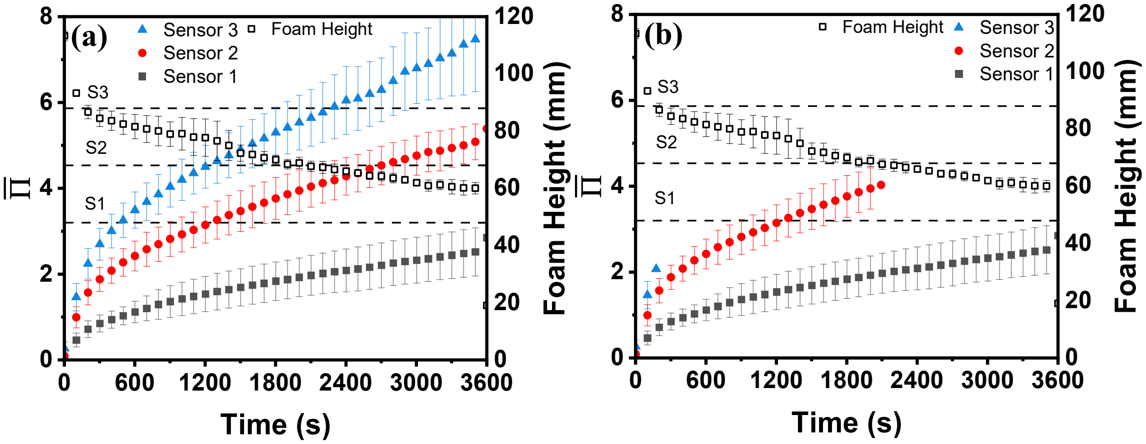

Figure 5.6. Osmotic Pressure as a function of time for 0.5 CMC SDS foam triplicates versus the overall foam height; (a) Full graph without removal of sensor data outside of foam height limits; (b) correcting the graph (a) to remove the calculated osmotic pressure points that reside outside the actual foam height data.

Shown in Fig. 5.6 is the $\overline{\Pi}$ of SDS over 3600 seconds as a function of sensor height within the foam. There is a clear stratification of $\overline{\Pi}$ as a function of height, from $\overline{\Pi} = 2.5$ at 48mm to $\overline{\Pi} = 7.5$ at 88mm at 3600s, which is a result of liquid drainage occurring from the top of the foam to the bottom. The $\overline{\Pi}$ also continuously increased over time showing that the surfactant had negligible impact on stabilizing the foam from liquid drainage. One ‘limit’ to the analysis of the $\overline{\Pi}$ was that the foam had to have not destabilized past the sensor height, or else the values obtained will be that of residual foam on the electrodes with air between them and would be aphysical. To take this into account, the foam height was plotted alongside the $\overline{\Pi}$ data. Once the actual foam height fell below these sensor heights, located as horizontal dashed lines on Fig. 5.6, the $\overline{\Pi}$ was removed to more accurately account for the destabilization and liquid drainage that occurred within the foam column. For example, the SDS foam quickly destabilized past the sensor 3 height, 88mm, and as such the $\overline{\Pi}$ data was limited to the first 200s, even though the sensor continued to record data as the residual foam on the electrodes collapsed and the overall $\overline{\Pi}$ approached that of air. This was then utilized to observe a particle foam system; Fig. 5.7 depicts $\overline{\Pi}$ for 0.5 – 2.0wt.% MSA – stabilized foam systems over 24 hours. At 0.5wt.%, the foam is unstable compared to those stabilized with higher particle concentrations, resulting in foam lasting up to 4 hours. This was represented by the limited $\overline{\Pi}$ values shown in Fig. 5.7a; the same stratification seen in the surfactant – stabilized system was also observed in this case. With increasing the particle concentration, the foam heights as well as the $\overline{\Pi}$ become more stable, and the overall slope of the $\overline{\Pi}$ was reduced. At the highest concentration, 2.0wt.%, the $\overline{\Pi}$ plateaued and at all sensor heights within the foam the values are approximately equal. This suggested two things: 1) There were enough particles in the foam solution to adequately cover the interfaces of all the bubbles to create a strong network which resulted in stable $\overline{\Pi}$ values with time and 2) gravity – assisted liquid drainage was halted in the entirety of the foam to a large degree so that the foam wetness was homogenous throughout. As shown by the liquid height graphs shown previously, liquid drainage did still occur in the foam over time but at a minimal degree comparatively to surfactant – stabilized foams. There was a stark contrast between the $\overline{\Pi}$ values for particle – stabilized foams and the surfactant – stabilized foams after an hour, with the surfactant foam being a magnitude larger, which indicated that the particles were able to better stabilize the foam against liquid drainage than a foaming agent.

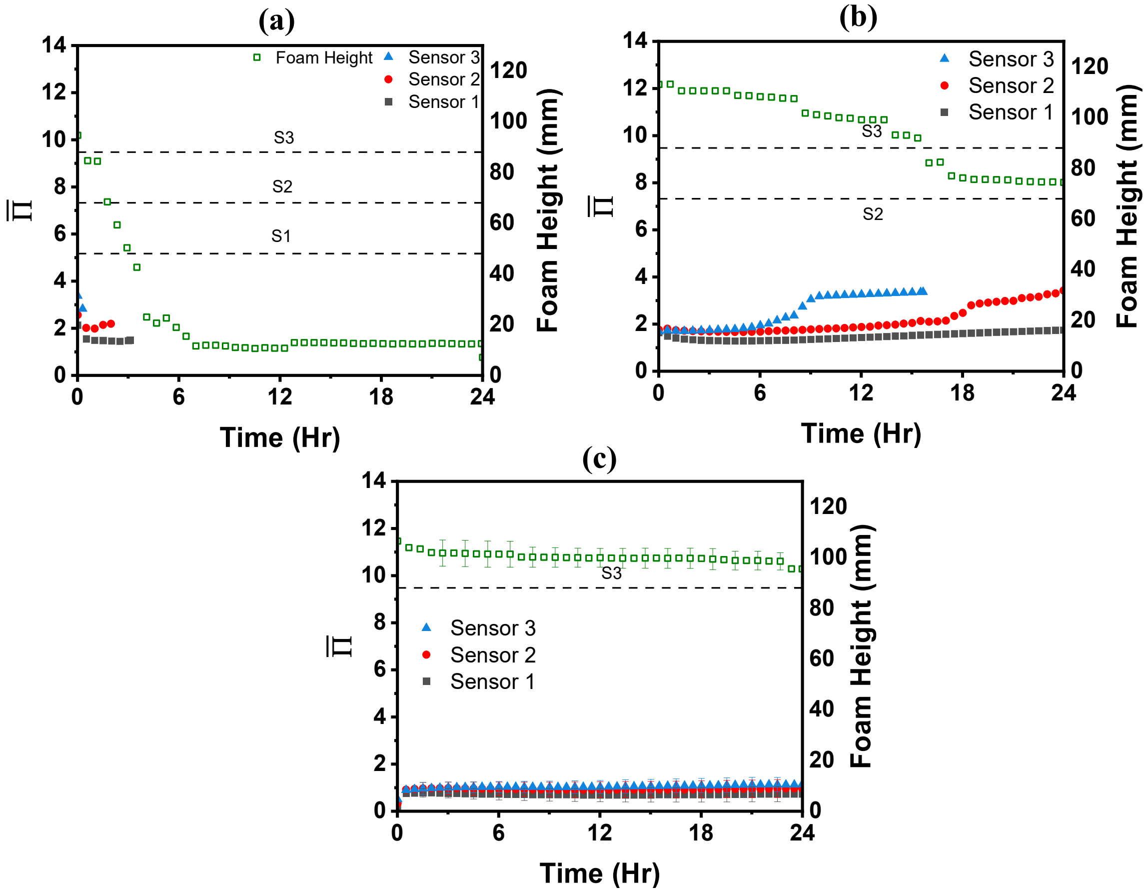

Figure 5.7. Osmotic pressure versus time for MSA particle – stabilized foam trials, with respect to foam height. (a) 0.5wt.%, (b) 1.0wt.%, and (c) 2.0wt.% MSA particles.

For the colloidal particle samples shown in Fig. 5.8, there are similarities to both surfactant – and fumed particle – stabilized foams over time. While, like surfactant, there are clear stratifications of the $\overline{\Pi}$ with time, the foam itself was also very stable against liquid drainage shown by the low slope of the $\overline{\Pi}$ which was akin to the fumed particle foams. It appeared that particles in general created foams that were more resistant to liquid drainage than surfactants; however, the colloidal particle foams had a slowly increasing $\overline{\Pi}$ unlike those of fumed particle foams in which drainage appears to be halted at higher concentrations.

This can be explained by the surface area that these particles possess. The colloidal particles had the lowest surface area of the particle species tested (SA = 10.5 m^2g^{-1}) and so when they bound themselves to the interface there was only a small amount of surface area that encroached into the lamellae of the foam. Due to this, the colloidal particles were unable to interact with much of the water in the lamellae outside of its small surface area protrusion, and thus liquid drainage occurred for the unhindered water, which caused the increased in the $\overline{\Pi}$ of the system. The fumed particles possessed much higher surface areas (MSA SA = 195 ± 20 m^2g^{-1}); these particles can expand and take up larger areas on the interface, shown via the AFM micrographs which signified that the fumed particle monolayer was noticeably smaller than the overall hydrodynamic diameter that was measured. This in turn meant that the fumed particles at the interface could expand and transmit a larger surface area into the lamella, which enabled them to interact and sterically hinder many more water molecules from draining due to gravity, leading to the plateaus shown in Fig. 5.7c. So, while the colloidal and fumed particles make similar amounts of long – lasting foam, they resist differently to the destabilization mechanisms that affect foams.

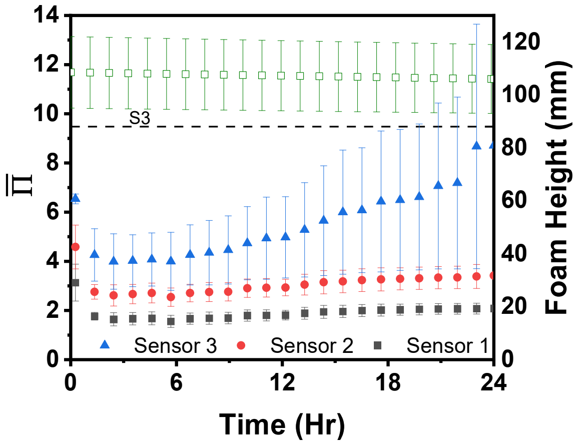

Figure 5.8. Osmotic pressure versus time for colloidal particle – stabilized foam trials, with respect to foam height (open square symbol) at 6.0wt.% colloidal particles.

5.3 Microstructure

Microstructure imaging can be an invaluable tool that allows for in – depth analysis of the foam itself to investigate how the bubble shape and size, and the resulting destabilization mechanisms can be impacted by various particle attributes. These images were obtained via light that was incident on a prism on the side of the foaming column which was refracted into the camera. Shown in Fig. 5.10 are some microstructure images for the SDS, fumed, and colloidal samples at varying times from 60s to 3600s after the foam generation. Starting with SDS, it can be seen that destabilization happened continuously over the hour as the thousands of small microbubbles eventually destabilized into a handful of much larger bubbles as shown in Fig 5.9 and Fig 5.10. The foam lamellas also visually decrease in size which corroborates the increase in the reduced osmotic

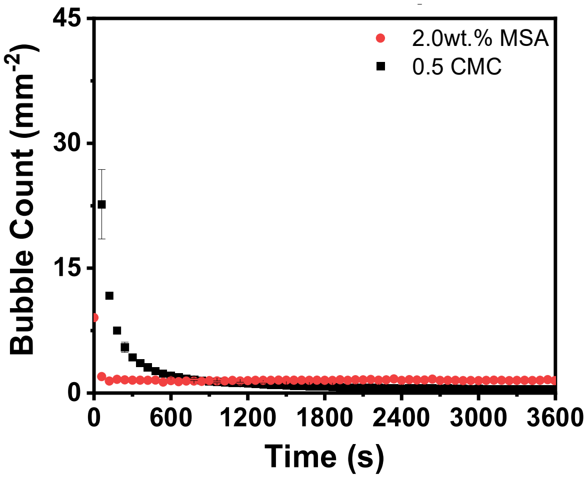

Figure 5.9. Comparison of bubble counts between 0.5 CMC SDS (black square) and 2.0wt.% MSA (red circle). The camera is in 1st position (~285mm^2 total area).

Pressure over time. For the fumed particle foam, it can be seen that the bubbles are much larger in size initially than those in the SDS foam and that there are fewer in numbers. However, unlike the SDS foam, the destabilization occurred only briefly, and the system appeared to resist further deformation and was very stable over the rest of the 3600s and for up to 109 hours after initial generation. The colloidal particle foam appeared to be very similar to that of the fumed foam. The initial bubbles were larger than the initial fumed bubbles, but as time elapsed they quickly became comparable in size. With regards to the liquid drainage, the colloidal foam drains much more quickly after the bubbles are stable as can be seen by the lamellae decreasing over the hour while the liquid drainage of the fumed particles halt after 600s. Both particle foams also have a rough texture compared to the SDS foams, due to the shell of particles that encapsulated the bubble surface and allowed for the enhanced stability overall. So, while visually the particle foams were similar and now only separated by the liquid drainage captured by the $\overline{\Pi}$, the rheological properties discussed in the following sections will distinguish the foams from each other in terms of their capabilities to resist interfacial stresses.

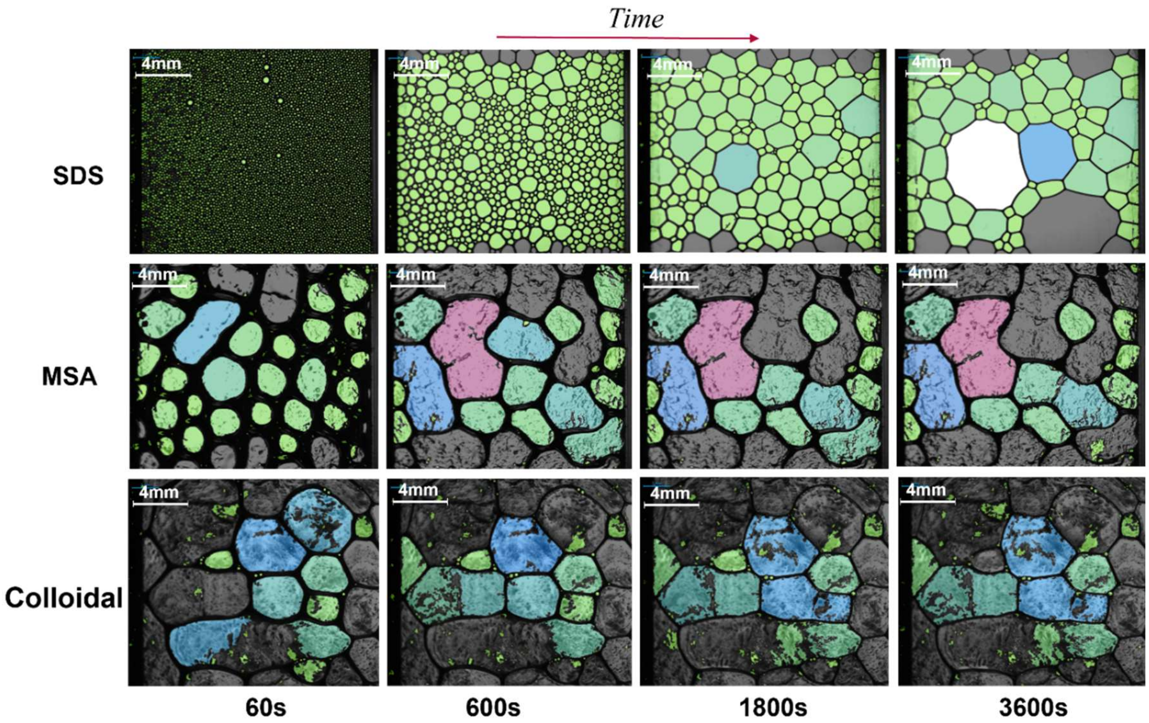

Figure 5.10. Comparison of microstructures captured for SDS and Pickering foams. Row 1) 0.5 CMC SDS – stabilized foams at 60, 600, 1800, and 3600s respectively; Row 2) MSA fumed silica particle – stabilized foams at 60, 600, 1800, and 3600s respectively; Row 3) Colloidal particle – stabilized foams at 60, 600, 1800, and 3600s respectively.

5.4 Mixed Systems: Surfactant & Particles

While particle – only systems can create very stable and long – lasting foams against coalescence and Ostwald ripening with similar foam heights, it is more common for solutions to contain both particles and surfactants. The particles effect is the same as mentioned previously, to help bubbles resist destabilization via the creation of an armored shell at the interface, while the surfactants assist with foam generation. In this regard, similar foam tests were conducted with MSA fumed silica particles at the most optimal concentration found in previous section, i.e., 2.0wt.%, mixed with SDS at 0.5 – 2.0 CMC.

The solutions were prepared following the same methodology discussed previously for the 2.0wt% MSA solutions and then left to evaporate for 2 – 3 days until the surface pressure was that of water. Afterwards, SDS was added to the solutions in order to generate the different CMC values. SDS was not added initially with the fumed silica as it would be difficult to observe whether the ethanol had been fully evaporated or not. These trials were then compared to both the 2.0wt% MSA trials as well as SDS – only trials at corresponding CMC values. Shown in Fig. 5.11 is the foam height versus time for mixed samples of 0.5 – 2.0 CMC compared to pure SDS samples at analogous CMC values. For SDS – only solutions with the preparation conditions, all the foam heights are similar and fall within the standard deviations of each other. Since the same amount of gas was injected into the solution, a similar amount of interfacial area would be generated and fully populated by the SDS molecules. However, when these concentrations of CMC were used with fumed silica particles, a difference in the foam height as well as stability over the hour could be noticed. Shown in Fig. 5.11b, the black line indicates the pure fumed silica trial, which exhibits a stable foam for the entire hour. When 0.5 and 1 CMC of SDS was added along with the fumed silica particles, a loss of stability is incurred onto the foam as the interfacial area was being occupied by surfactant molecules instead of solely particles. Up until 1 CMC, particles were still able to arrange themselves at the interface and make a weaker network, due to the stability of the mixed foams being less than that of pure particles but more than pure SDS. Once the CMC value was beyond 1, the interface appeared to be populated solely with SDS molecules as the foam height and stability were similar to that of a pure SDS solution shown in Fig. 5.11a. The SDS molecules are much more mobile than the particles and can more easily populate the interface of the foam, while the particles need the additional energy input via sparging to pin to the interface. With increased concentrations of SDS added, there is less surface area available for the fumed particles at the interface. In addition, the like charge of the SDS surfactant molecules and fumed silica particles reduced the ability for the fumed particles to adsorb onto the interface and create a network that enhanced the bubble stability. With the increase of SDS in the solution, the overall foam stability is reduced.

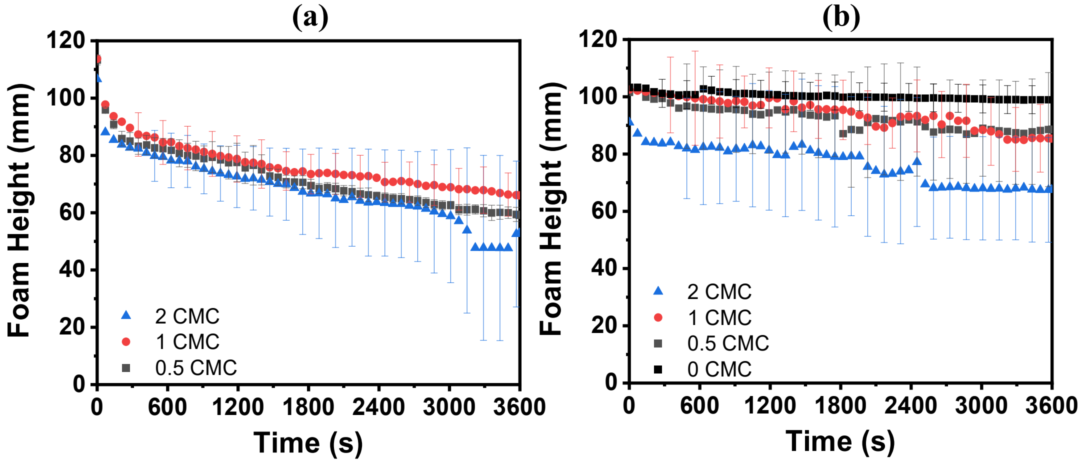

Figure 5.11. Foam height of (a) SDS – only solutions and (b) 2.0wt.% fumed silica and SDS solutions at varying SDS concentrations normalized by the CMC values.

With regard to how the osmotic pressures of these solutions change with SDS concentration, plotted below in Fig. 5.12 are the $\overline{\Pi}$ data for each system. It can be easily noticed that the mixed system at 0.5 CMC SDS has $\overline{\Pi}$ that is similar to a pure 2.0wt.% MSA solution which reiterated that the low amount of surfactant allowed for the population of fumed particles at the bubble interface leading to low amounts of liquid drainage. The 1.0 CMC/MSA solution has an $\overline{\Pi}$ shape profile that was akin to the pure 0.5 CMC SDS solution shown in Fig. 5.6, which illustrates the fact that at CMC the surfactants were able to populate the interface and prevent the interfacial binding of particles. As such, the liquid drainage of the system approached that of a pure SDS solution. When the SDS concentration was double the CMC value, the liquid drainage was much higher than either the 1.0 CMC/MSA solution or the pure 0.5 CMC solution. While the interface was still populated solely by surfactant, the lamellae was much more heavily filled with micelles. This increase in micelle concentration has been shown to decrease the overall elasticity of the interface and could influence and increase the drainage rate of the system, which ultimately affects the stability overall shown by the rapid foam height decrease of Fig. 5.11.

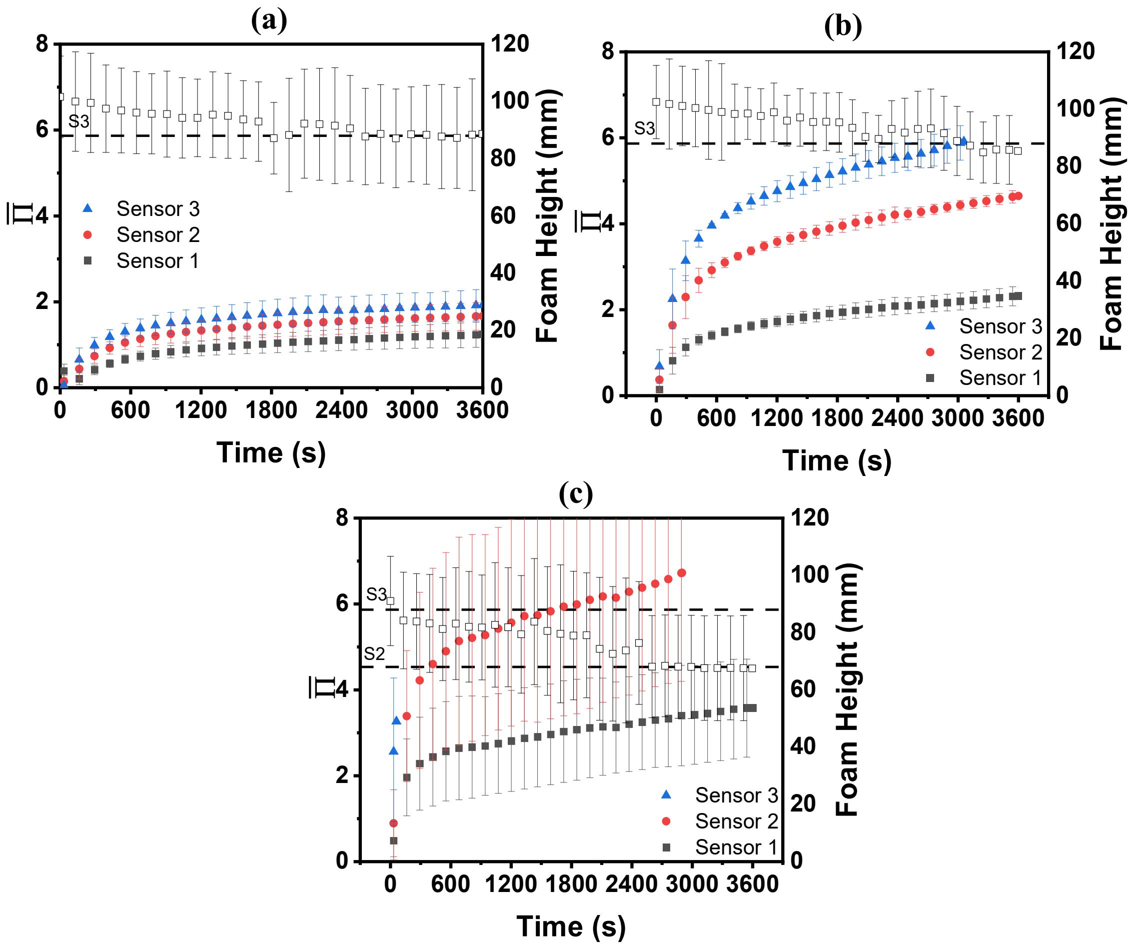

Figure 5.12. Osmotic pressure versus time for foams stabilized with mixed fumed silica/surfactant solutions at varying SDS concentration of (a) 0.5 CMC, (b) 1.0 CMC, and (c) 2.0 CMC; in all systems, the MSA particles are present at 2.0wt.%.

In order to estimate the rates of Ostwald ripening and coalescence in these mixed systems, the Lifshitz – Slyozov and Wagner Theory was used for Ostwald ripening in Eqn. 4, while Eqn. 5 was used to determine the coalescence rate.[95-99]

$$r_O t = \frac{64\gamma D_m V_m C_\infty t}{9RT} = d_t^3 - d_0^3 \qquad (4)$$

$$\frac{2\pi}{3} r_C t = \frac{1}{d_0^2} - \frac{1}{d^2} \qquad (5)$$

Where r_O is the rate of Ostwald ripening, r_C is the rate of coalescence, d is the Sauter mean diameter of the foam, γ is the interfacial tension, D_m is the molecular diffusion coefficient of the dispersed phase, V_m is the molar volume of the continuous phase, C_∞ is the solubility of the dispersed phase in the continuous phase, R is the gas constant, and t is time. Using these simple expressions, the rates of Ostwald ripening and coalescence with time were determined and then compared with regards to the CMC of SDS added to the system.

Fig. 5.13a & 5.13b show the Ostwald ripening rates for SDS – only and the mixed SDS – fumed system, respectively. With regards to the SDS – only graph, the rate of Ostwald ripening appeared to be similar for all the SDS. Concentrations studied. Because SDS is the only component in the system, which is very mobile and can exchange between the interface and bulk, Ostwald ripening was not being halted. For the mixed systems at 0.5 CMC, a visible change was seen in that the rate was much lower and increased in slope at a lower rate compared to the 1 & 2 CMC mixed trials. This reiterated what was discussed during the foam height portion, where at concentrations below 1 CMC the particles in the system were able to pin to the interface allowing for the formation of a particle network. This network prevented the diffusion of gas from the bubble to the foam lamellae as shown by the reduced rate over the hour. At higher SDS concentration of 1 CMC, SDS was the dominant species present at the interface, which caused the rates for the 1 & 2 CMC graphs to be almost identical to that of SDS – only trials shown in Fig. 5.13a.

Fig. 5.13c and 5.13d show the stability of foams against coalescence for the SDS – only and mixed systems, respectively. For the SDS – only systems, the main observation was that for concentrations below 1 CMC, the rates of coalescence were very similar between the CMC values. After 1 CMC, it appeared that the coalescence rate decreased, which could indicate that the system is more prone to Ostwald ripening as the 2 CMC rate in Fig. 5.13a was slightly larger than 0.5 & 1 CMC, however, the large standard deviation should be noted. With regards to the coalescence rates in mixed systems, the 0.5 CMC sample appeared to have the highest rate, while the 1 & 2 CMC trials exhibited lower rates. Due to the particles making the diffusion of gas more difficult, the bubbles would be more likely driven to coalesce instead and due to the weak nature of the particle network coalescence would be more easily achievable by the system. After the particles were unable to pin at the interface due to the large amount of surfactant available in the system at the higher CMC values, the rates went back towards SDS – only values.

Overall, it appeared that in systems of only SDS, both the Ostwald ripening and coalescence rates were more or less the same. While there were small deviations once 2.0 CMC was used that could represent rate – dependence on surfactant concentration at high micelle concentrations, it was difficult to differentiate due to the large standard deviations in the samples. For the mixed systems the results were more conclusive, in that, at lower CMC values the particles were able to adsorb to the interface and create a weak network that was stable against Ostwald ripening which caused the bubbles to preferentially chose coalescence, as the network was not strong enough to completely armor the bubbles against it. After the critical micelle concentration was met, the surfactants were the only species populating the interface and the characteristics of the Ostwald ripening and coalescence rates returned to those of SDS – only systems.

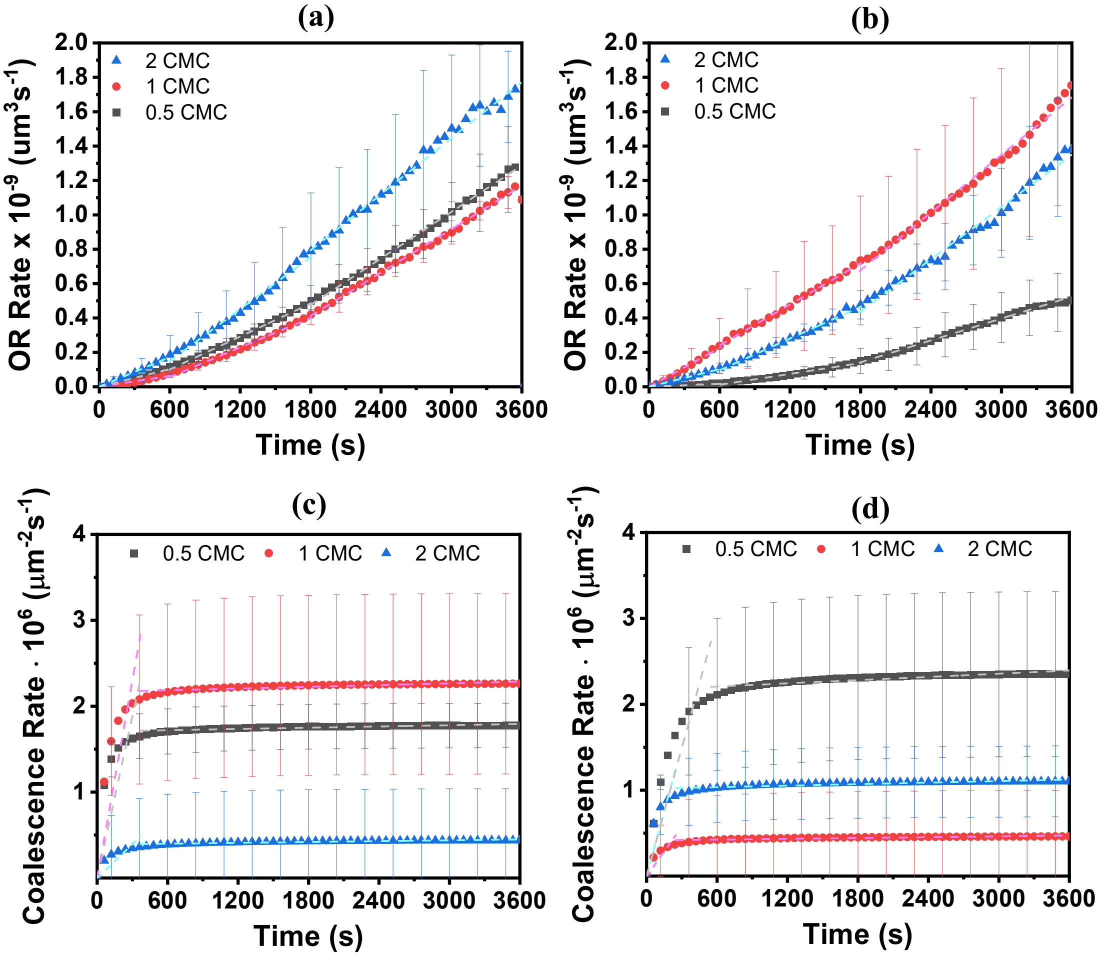

Figure 5.13. Rate of Ostwald ripening for SDS – only (a) and mixed systems (b); rate of coalescence for SDS – only (c) and mixed systems (d).

6. Interfacial Dilational Rheology

6.1 Droplet and Langmuir Trough Compressions

To investigate the interfacial networks of the particles and their ability to resist deformation and collapse, drop shape tensiometry was utilized. As discussed in the methods, a water droplet was formed on the tip of a needle, and then an ethanol solution containing the particles was deposited onto the droplet interface. From there, the droplet was compressed and pulsed in order to evaluate surface pressure changes and dilational rheological properties. In order to confirm whether the data obtained from this tensiometry was accurate, the Worthington and Bond numbers were utilized, discussed below in Appendix I. When the surface pressure as a result of droplet compression between the colloidal and fumed particle interfaces were compared in Fig. 6.1, they followed a similar linear increase towards a maximum of around 40 mN/m. However, when these particles were placed at the air/water interface on a Langmuir trough and then compressed it was seen that the fumed particles interact at longer ranges than the colloidal particles; as a result, the surface pressure changed more gradually for the fumed particles in response to the applied compression, whereas the surface pressure for the colloidal particle – laden interface increased starkly and over a narrower window of surface areas. The differences seen between the two equivalent compression tests could be due to the number of particles trapped at the interface, with less trapping occurred in the droplets compared to the trough. From the Langmuir trough compressions, it can be seen that the particles interact at different ranges depending on their surface attributes but overall, both reach similar maximum values of either ~40mN/m or ~70mN/m. The difference in interparticle interactions and the resulting particle network was exemplified when the droplets are oscillated allowing for measurements of the viscoelastic nature of the particle film.

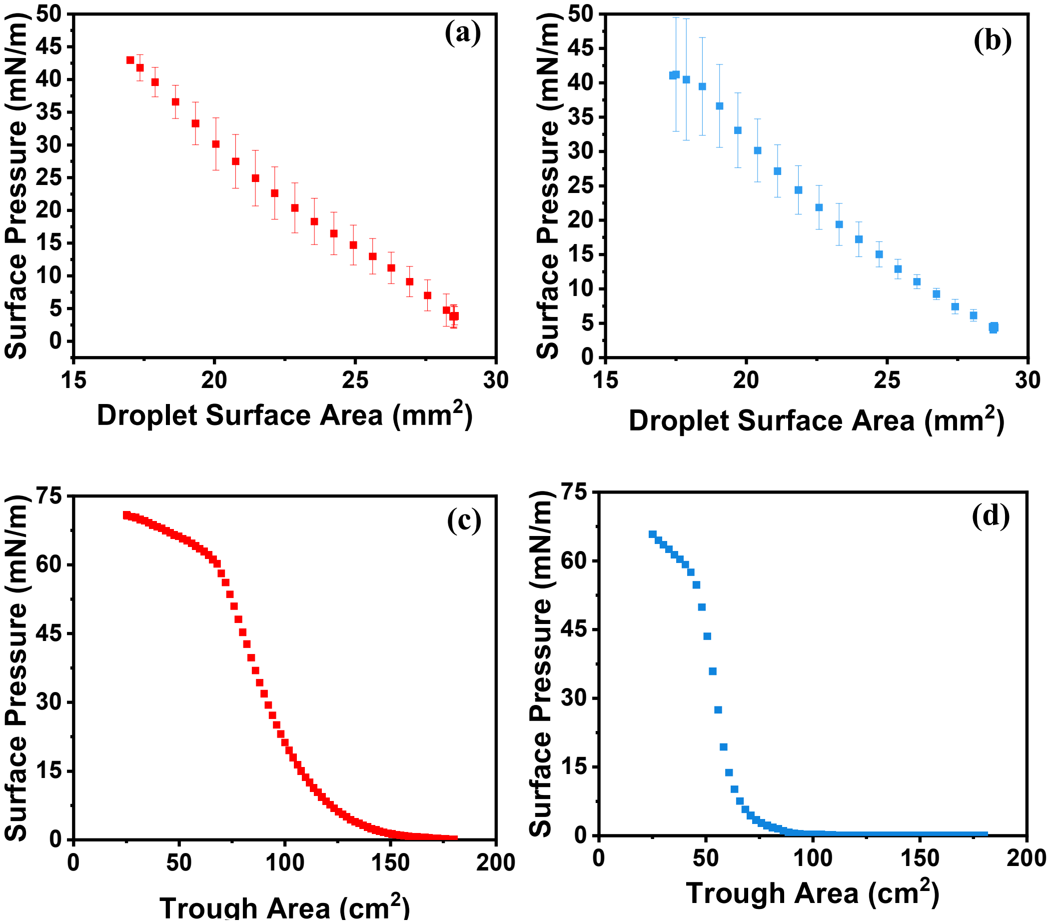

Figure 6.1. Compression isotherms obtained from droplet tensiometry for (a) 1.5mg MSA and (b) 3.75mg colloidal particles. Langmuir trough compression isotherms for (c) fumed and (d) colloidal particles.

6.2 MSA and Colloidal Dilational Elastic Moduli

By pulsing the droplet and changing the surface area, the change in the surface tension can be calculated using the Young – Laplace Equation shown below:

$$\gamma = \frac{\Delta P g R_0}{\beta} \qquad (6)$$

γ is the surface tension, ΔP is the Laplace pressure, g is gravity, R_0 is the radius of curvature of the droplet, and β is the shape factor of the droplet which is fitted. This equation is fit by the tensiometer software to determine the surface tension, and the complex elastic modulus E^* can be calculated by $E^* = \frac{\partial\gamma(t)}{\partial lnA(t)}$ where $\partial\gamma(t)$ is the change in surface pressure with time, and $\partial lnA(t)$ is the change in the natural log of the surface area with time. From E^* the elastic (E') and the viscous (E'') moduli can be calculated by:

$$E' = |E^*|\cos\delta \qquad E'' = |E^*|\sin\delta \qquad (7a \,\&\, 7b)$$

Where δ is the phase angle, which is the angular displacement between the surface tension and surface area curves as shown in Fig 6.2.

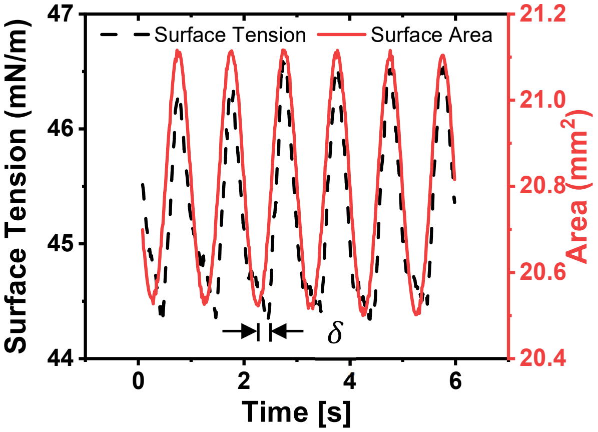

Figure 6.2. Surface tension and surface area curves with time, δ represents the phase angle between the two curves.

Fig. 6.3 shows E' as a function of surface pressure for both the MSA and colloidal particle networks. Both interfacial films have similar maxima of E' at around ~175 mN/m as well as having the maximum occur at near identical surface pressure values of ~15 mN/m, meaning that they are similar in elasticity, with E'' values (not shown) that are minimal. However, the extent to which the interface upholds this E' value was markedly different between the colloidal and fumed systems. The colloidal particles had a very steep slope to the maximum value and then after this critical surface pressure there was a similar steep downwards trend. The fumed particles on the other hand reached the E' maximum and then had a much slower descent back toward the lower E' values. This indicated that once the isotherm inflection point was reached, the colloidal particle network began to rapidly degrade and collapse, which caused the stark decrease in elasticity afterwards. In comparison, the fumed particle network could reach this inflection point and maintain a strong resistance to the interfacial deformation as the surface area decreased, which highlights the ability of the fumed particle network to maintain its structure through compressions most likely due to strong particle interactions and the particles' ability to rearrange at the interface. At higher surface pressures, and therefore lower areas and a more compressed state, the fumed network was much more resistant to deformation than the colloidal particle interface. Another aspect that can be used to gauge the stability of foams is the Gibbs stability criterion.[35, 55, 100] This criterion states that if the dilational elastic modulus E' is greater than $\frac{\gamma}{2}$, with γ being the interfacial tension, the resultant foam would be stable against Ostwald ripening due to the overall change in Laplace pressure of the system being equal to 0. Shown as the dark blue lines in Fig. 6.3, this stability criterion was met at all points by both the fumed and colloidal samples which further indicated that the particles led to stable foam unlike the SDS shown in A.2, which fell beneath this stability criterion for the entirety of the compression.[101]

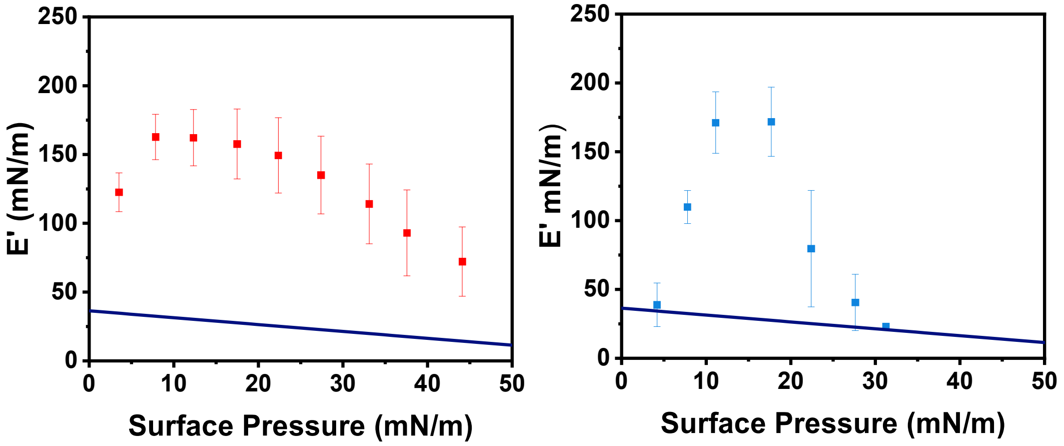

Figure 6.3. Dilational elastic modulus E' for interfacial networks of fumed silica (left) and colloidal silica (right) particles. The dark blue line represents the Gibbs stability criterion $E' > \frac{\gamma}{2}$.

6.3 Frequency and Concentration Dependence

The effect of frequency and concentration on dilational properties was also examined for the particles utilized. To determine the effect of concentration, a range from 0.5 – 2.0wt.% was utilized for the MSA, which was deposited onto the droplet interface as discussed above. After deposition the droplets were pulsated at increasing surface pressures until the droplet collapsed and the shape – fitting to the Young – Laplace equation was not valid. It can be observed in Fig. 6.4 that with increased concentration of particles deposited onto the interface, more surface pressures were available to enact pulsation tests for E' values, however the overall shape of the curve does not change. This meant that the same values obtained using 0.5wt.% concentration can be reached using 2.0wt.%, and that the only difference was that the higher concentration can be utilized to observe wider ranges of compression. From this, higher concentration solutions were utilized for both fumed and colloidal samples in order to generate larger curves that could be more easily compared as well as covering more of the overall particle network nuances as they alter with compression.

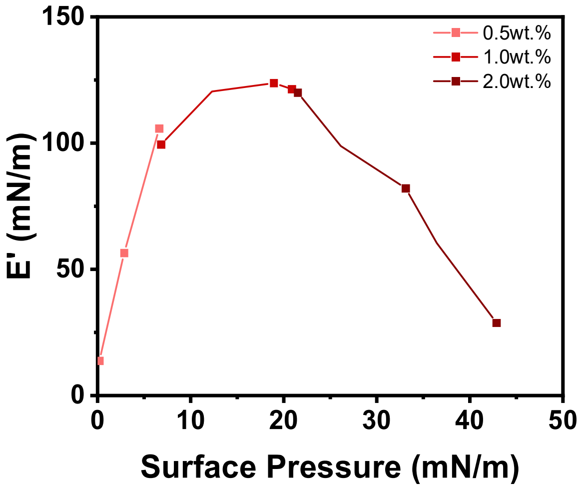

Figure 6.4. Dilational elastic modulus obtained at various surface pressures for interfacial network of MSA particles as a function of the initial solution concentration deposited on the pendant droplet surface.

The frequency at which the droplet was pulsed can alter the obtained E' values depending on the viscosity of the sample due to the available relaxation time the network has to recover.[102] It has been shown that with very high viscosity fluids, a lower frequency, such as 0.1 Hz, is necessary to completely capture the surface tension changes required to generate E^* and therefore E' and E'', whereas lower viscosity fluids can be handled with frequencies up to 1Hz.[78] Because of this, 0.1 and 1 Hz were used during droplet pulsations to examine the effect of oscillation frequency on the recorded elastic moduli for both fumed and colloidal networks. As can be seen in Fig. 6.5, for both fumed and colloidal samples, there appeared to be no dependence of E' on the applied frequency. For both particle types, the 0.1 and 1Hz overlapped or were within a very small range of each other, at most about a 30mN/m difference, which meant that the particle networks are able to relax fast enough for the correct E^* values to be obtained and that 1 Hz could be justified as an allowable frequency at which to pulse the droplets.

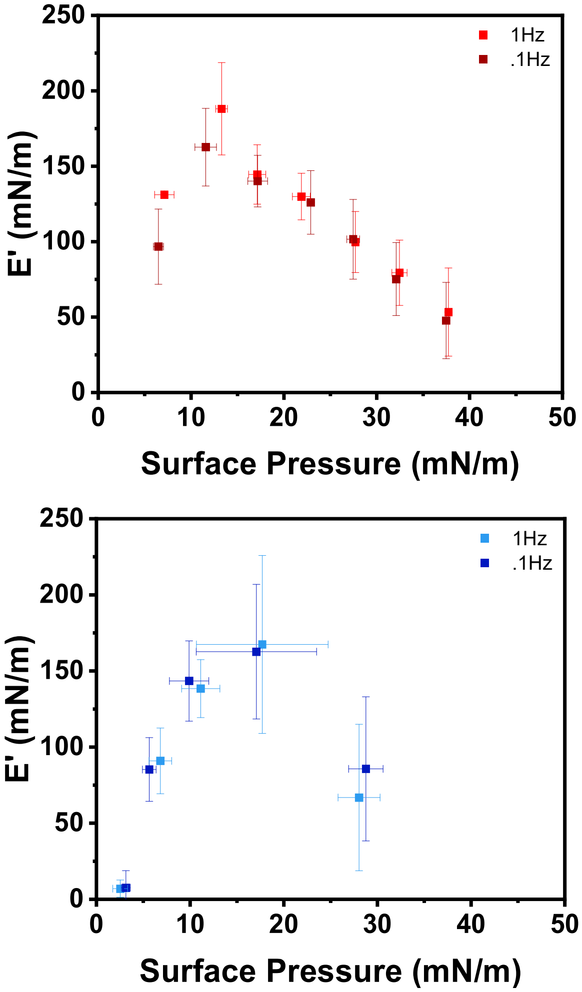

Figure 6.5. The frequency dependence of the dilational elastic moduli for interfacial networks of MSA (top) and colloidal (bottom) particles as a function of surface pressures.

6.4 Dilational Characteristics of the Interface and Foam Stability

To link the foam properties and interfacial dilatational properties, from the Langmuir trough compressions for the fumed and colloidal particle networks it was seen that the particles interact at different trough areas. The network of fumed particles resulted in a change in the surface pressure at ~150cm^2, while the colloidal particles caused surface pressure change at a~85cm^2, which signified that the fumed particles have longer ranged interactions, compared to the colloidal particles. A similar trend was shown by the E' plots where the fumed particle network had a broader range of E' values and was able to resist deformation at higher surface pressures in contrast with the colloidal particle network. These two observations can be linked to the imaged microstructure of foams as well as the recorded liquid drainage and overall foam stability. With regards to microstructure, the fumed particle foams appeared to destabilize initially to form larger bubbles that maintained their shape and stability for the remainder of the hour trials. The colloidal particle – stabilized foams however showed very limited signs of destabilization, i.e., Ostwald ripening or coalescence, during foaming and the bubbles remained a constant size from the onset of foaming until complete destabilization. This can be analyzed using the compression data shown in Fig. 6.1c, where the fumed silica has a slower initial slope during the compression. Because of this slower slope, the particles, albeit interacting at longer ranges, might not be in a well – formed network initially and would then be susceptible to rapid initial coalescence and Ostwald ripening until the network was fully formed on the bubble interfaces. With regards to stability, both particles show heightened elastic moduli which would enable them to maintain the polyhedral and non – spherical shapes shown in the microstructure images. The ability for the fumed foams to last upwards of 109 hours comes from its ability to maintain a high E' value at larger surface pressures, so while the foam is destabilized via liquid drainage the network is able to maintain its structure through heightened stress. Even after the foam had completely collapsed, particle shells were visibly seen remaining on the sides of the column and liquid content modules which shows the particle networks ability to remain even after complete destabilization shown in Fig. 6.6. While the interfacial network of colloidal particles had a sharper E' peak during the compression, the stresses put upon the network during foaming did not appear to surpass the networks' ability to maintain itself, as the colloidal foam was also very stable at long times, up to 96 hours.

Figure 6.6. MSA particle shell remains after foam trial completion.

7. Interfacial Shear Rheology

7.1 Amplitude Sweeps and Curve Fitting

Utilizing the DWR setup with Wilhelmy plate, the storage modulus (G') and loss modulus (G'') were gathered for both the colloidal and fumed interfacial networks at the air/water interface. First, amplitude sweeps at 1Hz were conducted to identify the strain % of the linear viscoelastic regime for both samples. Shown below in Fig. 7.1, it can be easily noticed that as the interface was compressed to reach larger surface pressures, the G' for both systems increase by about one order of magnitude from the 5mN/m to 30 – 40mN/m for interfacial networks of colloidal and fumed particles, respectively. The G' values for the fumed networks were about one order of magnitude lower than that of the colloidal interfacial films overall. With increased surface pressure, the overall coverage of particles on the interface increased. Therefore, the particles interacted with each other to a larger degree, which resulted in an increase in storage moduli for both particle types. One difference to note was that the overall range of increase of G' for the fumed network was less than that of the colloidal. This can be explained by the more amorphous nature of the fumed particles, which are able to alter their packing at the interface and can entwine with other particles at the interface or compress to a larger degree due to their flexible chains of primary silica particles. The colloidal particles, being rigid particles with a hard – sphere size, are not flexible and therefore led to larger changes in G' with compression.

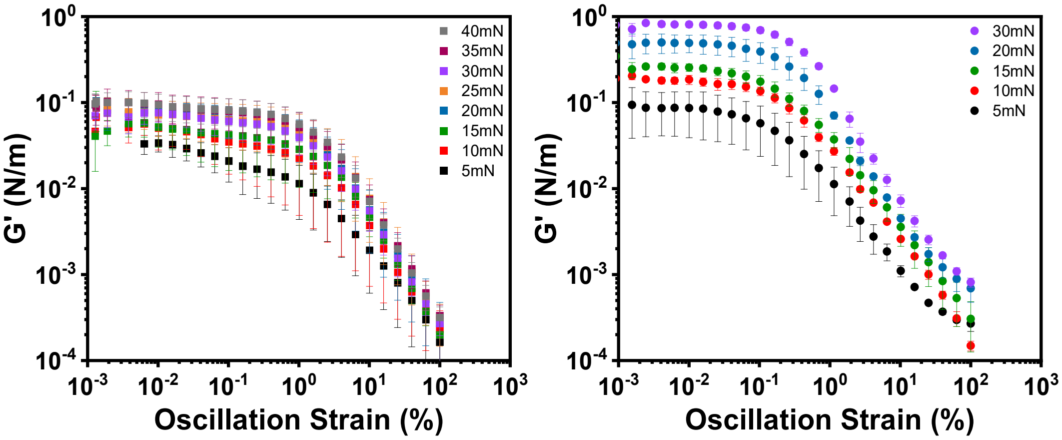

Figure 7.1. Amplitude sweeps performed at 1Hz for interfacial network of MSA (left) and colloidal (right) particles.

From the crossover points between a trendline of the linear regime and the high – strain non – linear regime, shown in Fig. 7.2, critical properties can be obtained and thus compared between the networks. The fittings were done by calculating the trendline for solely the linear regime (strain % < 0.1) and then a similar fit for points in the non – linear regime (strain % > 10).

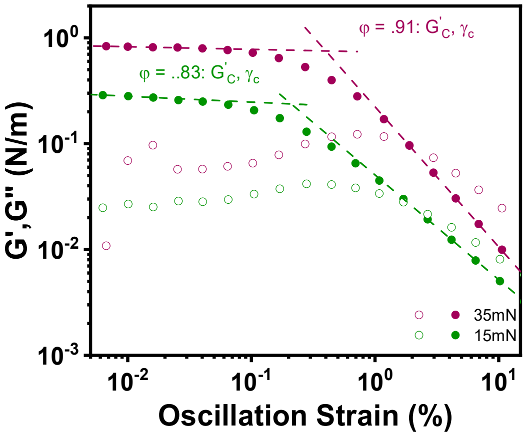

Figure 7.2. Fitting of critical parameters from the amplitude sweep data for a colloidal trial. G'_C is the critical storage modulus at which the curves tend towards the non-linear regime. γ_c is the critical strain at which G'_C takes place.

7.2 Frequency Sweeps and Frequency Dependence

Once the linear viscoelastic (LVE) regime was located for both particle samples, a strain % within the associated LVE range was utilized in frequency sweeps. The strain amplitude was set at 0.05% for both samples, and frequency analysis was conducted in the range of 10^{-2} to 10^2 Hz. These frequency trials were used to gather information on how the G' and G'' values change with frequency at different compression states, as well as highlight whether they have a solid – like or viscous – like network via their dependence on the frequency. Shown in Fig. 7.3, the trend was similar to the amplitude sweeps in that the G' for the colloidal network tends to be an order of magnitude larger than the fumed network. This reiterated the previous statements that the fumed particles create a network with a lower elastic modulus compared to that of the colloidal network. The larger range over which the fumed particles maintained an elastic network also mimics the amplitude sweeps, which alluded to the similar explanation of the fumed particles being able to compress and rearrange at the interface more so than the colloidal particles. When the dependence of the fumed and colloidal networks with frequency was examined, power law trendlines were plotted and the exponents were compared. It has been shown that when the exponent of the G' frequency dependence approached 1, i.e., $G' = A\omega^B, B = 1$, then the network was viscous dominated and if it approached 0 then it was elastic dominated or more solid – like.[80] The fumed networks exponents were initially around 0.06 and decreased with increasing surface pressure to around 0.04 for the largest surface pressure analyzed, while the colloidal frequency dependence remained around 0.04 with increased surface pressure. This meant that the fumed networks are slightly more viscous – like initially, while the colloidal particles are slightly less dependent on the viscous subphase through the entire compression. Overall, however, both interfaces were firmly solid – like as the dependence was much less than 1. The fumed have been shown to have longer ranged particle – particle interactions than the colloidal particles, so this viscous element is most likely caused by a lack of a strong network being formed at low surface pressures. The dependence of G'' with frequency was also analyzed; the fumed particles had dependencies that varied between 0.03 and -0.06 as the surface pressure was increased. Because of this varied dependence, the G'' of the fumed interface was most likely not dependent on the frequency. The colloidal network had dependencies that started initially at -0.09 at 5mN/m, and increased to -0.07 at 35mN/m. The negative sign of the frequency dependence signified that the monolayer became more solid – like with increased compression, as the G'' represented the viscous nature of the interface.

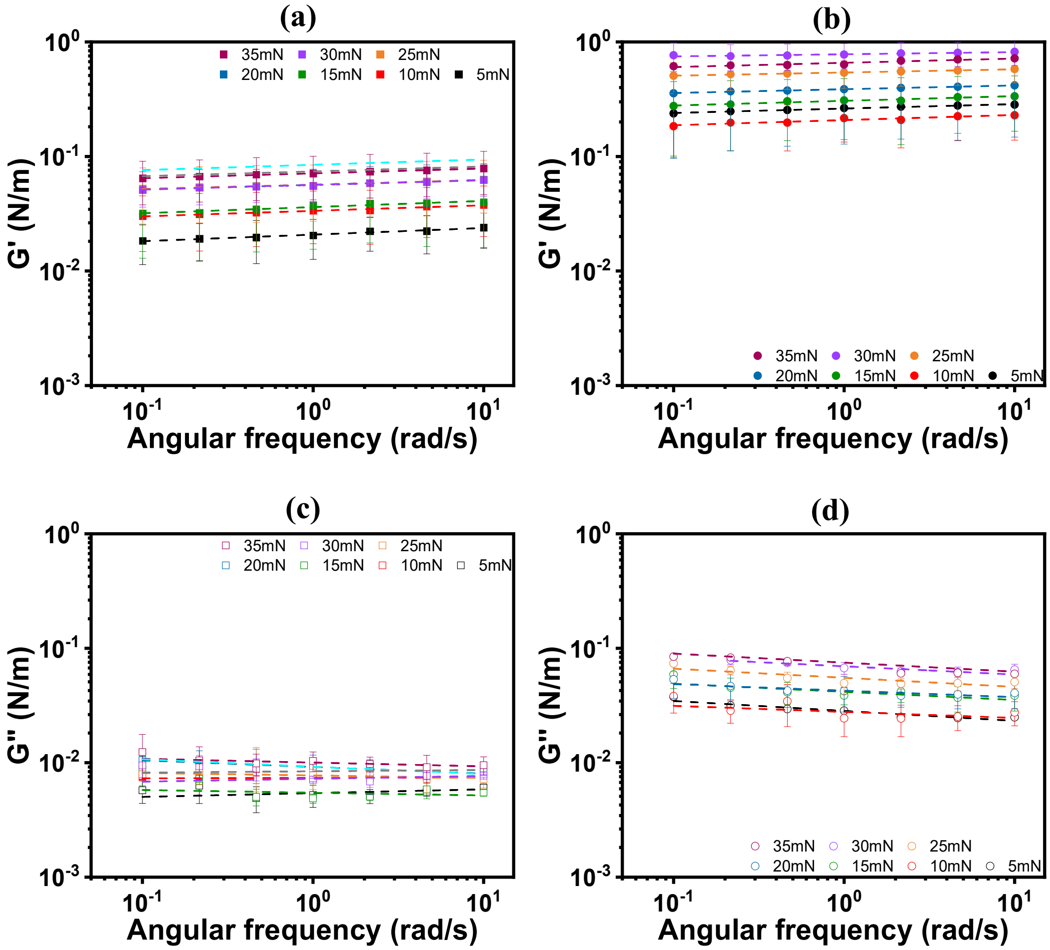

Figure 7.3. G' and G'' data and the corresponding fits obtained from interfacial shear frequency sweeps spanning from 5 – 35 mN/m surface pressures, at 0.005% over 0.02 – 10 Hz for (a), (c) fumed and (b), (d) colloidal particle networks.

7.3 Surface Coverage Calculations

In previous sections, the rheological properties such as E' or G' were given with regards to the surface pressure at which they were determined. However, a more applicable and translatable scale would be to have these characteristics as a function of surface coverage, or the amount of surface area occupied by the particles during compression. In order to generate the information on the coverage, multiple images were taken at different surface pressures. The images were then manually thresholded in ImageJ from which the particle fraction could be determined. Shown below is a sample procedure in which an interfacial image is thresholded and then used to determine the surface coverage.

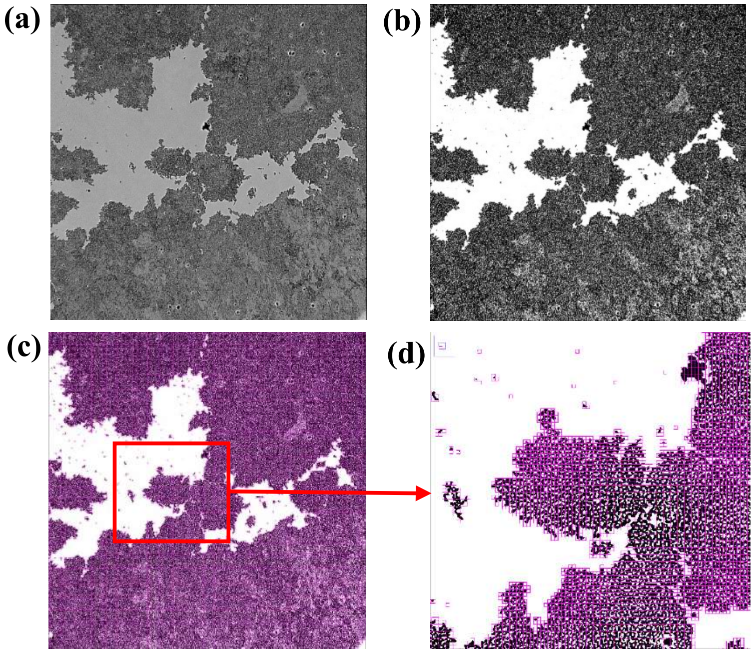

Figure 7.4. Image conversion and analysis for particle coverage and fractal dimensions. (a) Base image; (b) thresholded black & white of the base image; (c) thresholded base image run through FracLac for fractal box counting; (d) zoomed in image of the boxes on the base image.

From the previously shown thresholded image, the coverage can be calculated and graphed versus surface pressure as shown in Fig. 7.5a. With increased compression, it was expected that the surface coverage of the particle network would increase as the particles are pushed closer together, resulting in an increase of the surface pressure. This increase in coverage continued until the inflection point of the particle network, the point at which the network can no longer withstand the applied compressions. Upon any further compression, the monolayer collapsed by either wrinkling, multilayer formation, or particle ejection into the bulk. The closest random packing that can be obtained for spheres is 0.89 in two – dimensional space. From Fig. 7.5a, the inflection point, the surface tension where the coverage surpasses 0.89, appears to be around 33mN/m for the colloidal particles which was similar to the inflection point, calculated from graphically fitting Fig. 6.1c, ~31.9mN/m. With regards to fumed particle networks at the interface the inflection point appeared to be around 15mN/m, which was much lower than the inflection point fitted from Fig. 6.1d, ~36.7mN/m. The fitted inflection points were obtained from graphical analysis of the compression isotherms in Fig. 6.1 and were located where the slope of the increasing surface pressure changed. However, the inflection point shown below was obtained via image analysis of when the onset of wrinkling was seen in the compression video. As discussed, wrinkling signifies the onset of the inflection point as the interface was no longer a singular monolayer. This large difference could then be attributed to the fumed particle's ability to rearrange at the interface. Since the particles spread out at the interface, shown via AFM imaging, they fully pack much faster than the colloidal particles did, which would allude to the lower inflection point. However, because of the chain flexibility and rearrangement, the fumed particles might be able to be continually compressed until, at the later inflection point, they are unable to compress further and begin to form multilayers. When the colloidal inflection point was determined using the wrinkle-onset method shown in Fig 7.5b, the values obtained were very similar to those found from image analysis. This gave weight to the previous determined MSA inflection point, as well as reflected the hard nature of the colloidal particles, which are unable to rearrange like the MSA chains, causing wrinkling to occur at maximum packing of the interface. Ultimately, the lower inflection point was chosen as the most likely MSA candidate due to the ambiguous nature of how these particles compress and rearrange at the interface.

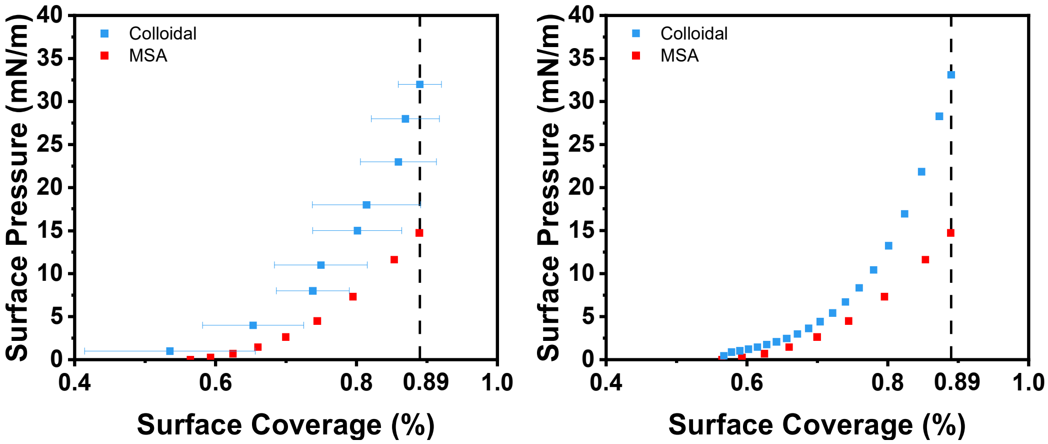

Figure 7.5. Calculated surface coverage for fumed and colloidal interfaces during compression as a function of surface pressure. MSA coverage calculated backwards from the inflection point, and colloidal coverage calculated from image analysis obtained from imaging the interface at each surface pressure listed (left); Surface coverages calculated backwards from the inflection point for both interfaces (right).

7.4 Interfacial Shear Rheology Properties

The critical shear properties obtained via the crossover of the linear and non – linear trendlines are shown in Fig. 7.6. First, it can be seen that the critical strain γ_c increased for both fumed and colloidal particle networks with increased surface coverage; the networks, at increased coverage, required more strain to break and enter the non – linear regime. This was due to the increased particle interactions at higher surface coverages as they were being forced closer together. The critical strain of the fumed particle network was also consistently higher than that of the colloidal particles, which resembles the E' graphs shown earlier (Fig. 6.4). Similar to the dilational case, the fumed particles created networks that seemed to resist deformation to a larger degree than the colloidal particles, even though the colloidal had larger G' values than the fumed networks. When examining the critical G' value, or the G' value at which the graph began to trend into the non – linear regime, it can be seen that the colloidal and fumed have markedly different trends. The fumed critical G'

increased very slowly with increased surface coverage. While the surface coverage increased from 75% to 89%, the G' did not increase to the same degree as the colloidal particles. This exemplified that the fumed particles are able to rearrange within the network as they are compressed, unlike the colloidal particles with the much steeper slope of increasing critical G' with coverage. Lastly, the yield point, or yield stress, versus surface coverage is plotted. The yield stress, which can be calculated by $Y_p = G' \cdot \gamma_c$, defines the stress necessary to break the solid network and cause the surface to flow like a fluid. As seen from the graph, the colloidal particle network had a higher yield stress over the range of surface coverages, but all together was very similar to the fumed particles. This meant that the interfacial network of colloidal particles required slightly more stress to break compared to the network formed by the fumed particles.

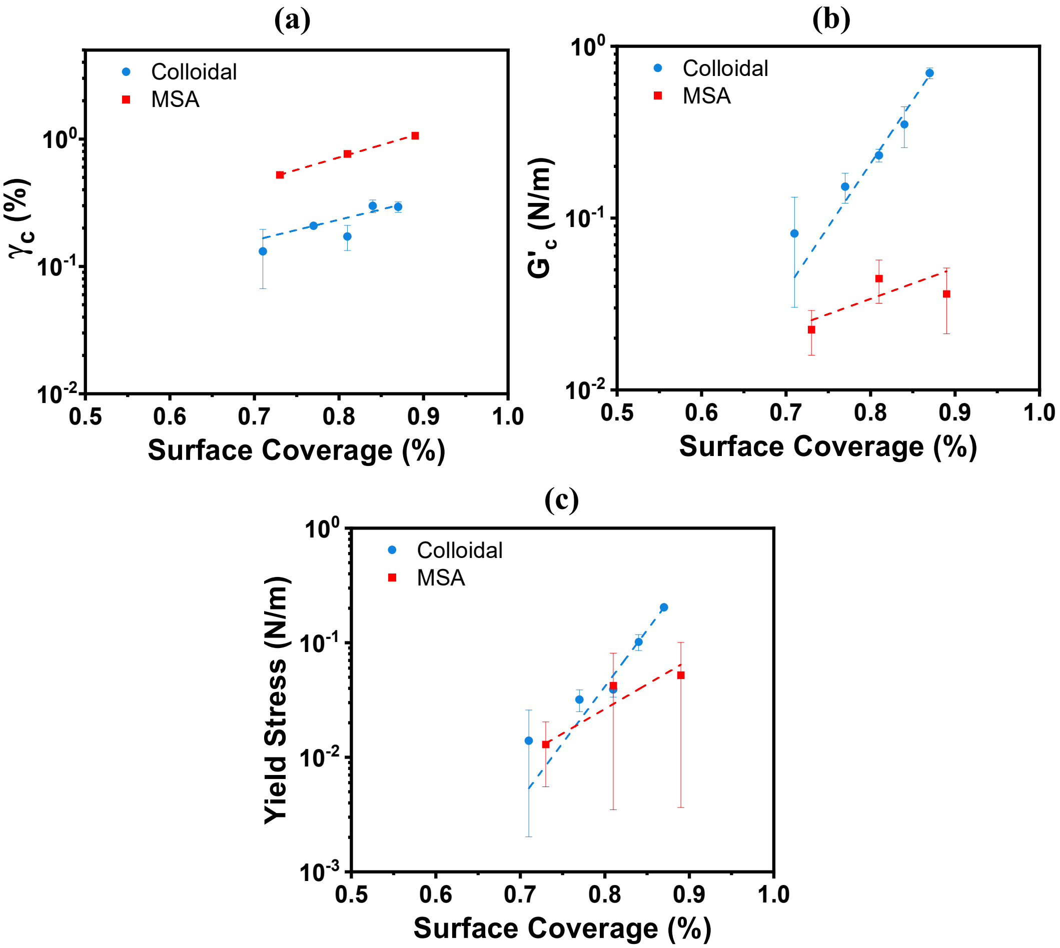

Figure 7.6. (a) critical strain, (b) critical elastic modulus at yield, and (c) yield stress of the interfacial networks as a function of the particle surface coverage for both networks formed by the colloidal and fumed particles.

8. Conclusions and Outlook

In summary, we have compared particle – stabilized foams and their ability to resist destabilization compared to common foaming agents such as SDS. Furthermore, we have investigated the impact of fumed silica versus colloidal silica particles and how particle roughness can alter the foam characteristics and rheological properties. The fumed particles showed an apparent linear dependence of half – life on concentrations which persisted upwards of 2.0wt.% of particles, meaning that specific foam half – lives could be picked based on necessity which allows for more tunable foam in many situations. Fumed and colloidal particles both stabilize the foam against destabilization mechanism such as coalescence and Ostwald ripening leading to much longer foam half – lives compared to SDS – stabilized foams. We also investigated the use of osmotic pressure and how it can be employed as a tool to examine the impact of particle type on the liquid drainage and foam stability. One major difference between the two particle systems was their control on the liquid drainage, and it was observed that the fumed silica particles resisted liquid drainage to a larger degree than colloidal particles, which was attribute to their increased surface area leading to a larger ability to interact and hinder water movement through the foam lamellae. Mixed systems were also studied to show the effect of particles with surfactant; it was established that once the surfactant concentration surpassed the CMC, the resultant foam properties were akin to SDS – only systems. With regard to the microstructure, we have observed the impact of particles on resisting destabilization mechanisms visually compared to SDS. Both particle systems fully encapsulate the bubbles leading to an armor that halts diffusion at higher concentrations and resisted coalescence. Both dilational and shear rheological properties were investigated between the colloidal and fumed systems to analyze their elastic capabilities and their resistance to interfacial deformation. It was found that both particles have similar maxima in E' and thus are similarly resistant to dilational deformation; however, the fumed particles maintain this resistance over a much broader surface pressure spectrum, and thus compression states, than that of colloidal particles. Shown via the Gibbs modulus, both the fumed and colloidal systems are above the criteria required for cessation of coarsening, which reiterated what was shown visually in the imaged foam microstructure. With regards to interfacial shear rheology, it was shown that the colloidal particles had higher G' values through both frequency and amplitude sweeps by an order of magnitude than what was seen in the fumed network. Because the fumed network showed a diminished increase in yield stress, critical G', and critical strain % compared to the rigid colloidal particles, it is thought that the fumed particles are able to compress and rearrange more easily at the interface via their amorphous structure, which was highlighted by the AFM imaging that showed the thickness of the interfacial network of fumed particles were less than that of their hydrodynamic diameter in bulk. This enabled the fumed particles to make strong networks much like the colloidal particles, with more structural resilience during increased compressions through the heightened particle and chain interactions. The colloidal particles, with their larger G'' values, would be stronger against shearing and should create a foam more resistant to outside influence than the fumed particles which are more suited to resisting forces such as gas diffusion and liquid drainage. Overall, the particles have shown to create elastic networks at the air/water interface that helped form foams that were resistant to destabilization mechanisms and increased the half – life of the foam more so than foaming agents but vary in their abilities to maintain networks for long periods of time against increased stress and liquid drainage. These findings will be of use in many applications; by understanding the connections between foam stability and their rheological properties, specific solutions can be prepared to fit the necessary requirements. As can be seen, particle foams may have very similar stability but simultaneously behave differently with regard to drainage as well as its network strength. By combining these factors, more properly tuned foams can be achieved.

References

1. Ferreira, F. V.; Otoni, C. G.; De France, K. J.; Barud, H. S.; Lona, L. M. F.; Cranston, E. D.; Rojas, O. J., Porous nanocellulose gels and foams: Breakthrough status in the development of scaffolds for tissue engineering. *Materials Today* **2020,** *37*, 126-141.

2. Chen, L.; Zhou, X.; He, C., Mesoporous silica nanoparticles for tissue-engineering applications. *Wiley Interdiscip Rev Nanomed Nanobiotechnol* **2019,** *11* (6), e1573.

3. Kim, M. Y.; Kim, J., Chitosan Microgels Embedded with Catalase Nanozyme-Loaded Mesocellular Silica Foam for Glucose-Responsive Drug Delivery. *ACS Biomaterials Science & Engineering* **2017,** *3* (4), 572-578.

4. Yoon, I.-H.; Kim, S. E.; Choi, M.; Kim, S.; Choi, W.-K.; Jung, C.-H., Highly enhanced foams for stability and decontamination efficiency with a fluorosurfactant, silica nanoparticles, and Ce(IV) in radiological application. *Environmental Technology & Innovation* **2020,** *18*, 100744.

5. Andrieux, S.; Quell, A.; Stubenrauch, C.; Drenckhan, W., Liquid foam templating – A route to tailor-made polymer foams. *Advances in Colloid and Interface Science* **2018,** *256*, 276-290.

6. Etemad, S.; Kantzas, A.; Bryant, S., Experimental investigation of CO2 foam stability enhancement by partitioning particles. *Journal of Petroleum Science and Engineering* **2020,** *194*, 107540.

7. Yu, H.; Zhu, Y. F.; Hui, A. P.; Yang, F. F.; Wang, A. Q., Removal of antibiotics from aqueous solution by using porous adsorbent templated from eco-friendly Pickering aqueous foams. *Journal of Environmental Sciences* **2021,** *102*, 352-362.

8. Calhoun, S. G. K.; Chandran Suja, V.; Fuller, G. G., Foaming and antifoaming in non-aqueous liquids. *Current Opinion in Colloid & Interface Science* **2022,** *57*, 101558.

9. Matis, K. A.; Mavros, P., Foam/Froth Flotation. *Separation and Purification Methods* **1991,** *20* (2), 163-198.

10. McCoy, T. M.; Parks, H. C. W.; Tabor, R. F., Highly efficient recovery of graphene oxide by froth flotation using a common surfactant. *Carbon* **2018,** *135*, 164-170.

11. Amirsadat, S. A.; Moradi, B.; Hezave, A. Z.; Najimi, S.; Farsangi, M. H., Investigating the effect of nano-silica on efficiency of the foam in enhanced oil recovery. *Korean Journal of Chemical Engineering* **2017,** *34* (12), 3119-3124.

12. Lu, T.; Li, Z.; Zhou, Y., Flow Behavior and Displacement Mechanisms of Nanoparticle Stabilized Foam Flooding for Enhanced Heavy Oil Recovery. *Energies* **2017,** *10* (4), 560.

13. Chaturvedi, K. R.; Sharma, T., In-situ formulation of pickering CO 2 foam for enhanced oil recovery and improved carbon storage in sandstone formation. *Chemical Engineering Science* **2021,** *235*.

14. Wanniarachchi, W. A. M.; Ranjith, P. G.; Perera, M. S. A.; Lashin, A.; Al Arifi, N.; Li, J. C., Current opinions on foam-based hydro-fracturing in deep geological reservoirs. *Geomechanics and Geophysics for Geo-Energy and Geo-Resources* **2015,** *1* (3), 121-134.

15. Hematpur, H.; Mahmood, S. M.; Nasr, N. H.; Elraies, K. A., Foam flow in porous media: Concepts, models and challenges. *Journal of Natural Gas Science and Engineering* **2018,** *53*, 163-180.

16. Zhou, H.; Qu, C.; Lu, G.; Li, Z.; Wang, X.; Yin, H.; Feng, Y., Deliquification of Low-Productivity Natural Gas Wells with In Situ Generated Foams and Heat. *Energy Fuels* **2021,** *35* (12), 9873-9882.

17. Britan, A.; Liverts, M.; Ben-Dor, G.; Koehler, S. A.; Bennani, N., The effect of fine particles on the drainage and coarsening of foam. *Colloids and Surfaces A: Physicochemical and Engineering Aspects* **2009,** *344* (1), 15-23.

18. Pawar, A. B.; Caggioni, M.; Ergun, R.; Hartel, R. W.; Spicer, P. T., Arrested coalescence in Pickering emulsions. *Soft Matter* **2011,** *7* (17), 7710-7716.

19. Beltramo, P. J.; Gupta, M.; Alicke, A.; Liascukiene, I.; Gunes, D. Z.; Baroud, C. N.; Vermant, J., Arresting dissolution by interfacial rheology design. *Proceedings of the National Academy of Sciences* **2017,** *114* (39), 10373-10378.

20. Princen, H. M.; Kiss, A. D., Osmotic pressure of foams and highly concentrated emulsions. 2. Determination from the variation in volume fraction with height in an equilibrated column. *Langmuir* **1987,** *3* (1), 36-41.

21. Stocco, A.; Drenckhan, W.; Rio, E.; Langevin, D.; Binks, B. P., Particle-stabilised foams: an interfacial study. *Soft Matter* **2009,** *5* (11), 2215-2222.

22. Höhler, R.; Seknagi, J.; Kraynik, A., Capillary pressure, osmotic pressure and bubble contact areas in foams. *Soft Matter* **2021,** *17* (29), 6995-7003.

23. Oetjen, K.; Bilke-Krause, C.; Madani, M.; Willers, T., Temperature effect on foamability, foam stability, and foam structure of milk. *Colloids and Surfaces A: Physicochemical and Engineering Aspects* **2014,** *460*, 280-285.

24. Yang, L. L.; Wang, T. D.; Yang, X.; Jiang, G. C.; Luckham, P. F.; Xu, J. P.; Li, X. L.; Ni, X. X., Highly Stabilized Foam by Adding Amphiphilic Janus Particles for Drilling a High-Temperature and High-Calcium Geothermal Well. *Industrial & Engineering Chemistry Research* **2019,** *58* (23), 9795-9805.

25. Taherpour, A.; Hashemi, A., A novel formulation of the pickering emulsion stabilized with silica nanoparticles and its thermal resistance at high temperatures. *Journal of Dispersion Science and Technology* **2018,** *39* (12), 1710-1720.

26. Amiri, A.; Øye, G.; Sjöblom, J., Influence of pH, high salinity and particle concentration on stability and rheological properties of aqueous suspensions of fumed silica. *Colloids and Surfaces A: Physicochemical and Engineering Aspects* **2009,** *349* (1), 43-54.

27. Alzobaidi, S.; Da, C.; Wu, P.; Zhang, X.; Rabat-Torki, N. J.; Harris, J. M.; Hackbarth, J. E.; Lu, C.; Hu, D.; Johnston, K. P., Tuning Nanoparticle Surface Chemistry and Interfacial Properties for Highly Stable Nitrogen-In-Brine Foams. *Langmuir* **2021,** *37* (17), 5408-5423.

28. Katepalli, H.; John, V. T.; Tripathi, A.; Bose, A., Microstructure and rheology of particle stabilized emulsions: Effects of particle shape and inter-particle interactions. *Journal of Colloid and Interface Science* **2017,** *485*, 11-17.

29. Alzobaidi, S.; Lotfollahi, M.; Kim, I.; Johnston, K. P.; DiCarlo, D. A., Carbon Dioxide-in-Brine Foams at High Temperatures and Extreme Salinities Stabilized with Silica Nanoparticles. *Energy Fuels* **2017,** *31* (10), 10680-10690.

30. Subinuer Yilixiati, R. R., Yiran Zhang, Vivek Sharma, Effect of Salt on Drainage Via Stratification in Micellar Foam Films. **2017**.

31. Khajehpour, M.; Reza Etminan, S.; Goldman, J.; Wassmuth, F.; Bryant, S., Nanoparticles as Foam Stabilizer for Steam-Foam Process. *SPE Journal* **2018,** *23* (06), 2232-2242.

32. Tengku Mohd, T. A.; Noor Fitrah, A. B.; Awang, N.; Talib, A., Aqueous foams stabilized with silica nanoparticle and alpha olefin sulfonates surfactant. *Journal of Mechanical and Engineering Sciences* **2018,** *12*, 3759-3770.

33. Tyowua, A. T.; Binks, B. P., Growing a particle-stabilized aqueous foam. *Journal of Colloid and Interface Science* **2020,** *561*, 127-135.

34. Yao, X.; Zhao, G.; Dai, C.; Wu, Y.; Lyu, Y., Interfacial characteristics and the stability mechanism of a dispersed particle gel (DPG) three-phase foam. *Journal of Molecular Liquids* **2020,** *301*, 112425.

35. Cervantes Martinez, A.; Rio, E.; Delon, G.; Saint-Jalmes, A.; Langevin, D.; Binks, B. P., On the origin of the remarkable stability of aqueous foams stabilised by nanoparticles: link with microscopic surface properties. *Soft Matter* **2008,** *4* (7), 1531-1535.

36. Hurtado, Y.; Franco Ariza, C.; Riazi, M.; Cortés, F., Improving the stability of nitrogen foams using silica nanoparticles coated with polyethylene glycol. *Journal of Molecular Liquids* **2019,** *300*, 112256.

37. Vishal, B.; Ghosh, P., The effect of silica nanoparticles on the stability of aqueous foams. *Journal of Dispersion Science and Technology* **2019,** *40* (2), 206-218.

38. Denkov, N.; Tcholakova, S.; Politova-Brinkova, N., Physicochemical control of foam properties. *Current Opinion in Colloid & Interface Science* **2020,** *50*, 101376.

39. Bindal, S. K.; Sethumadhavan, G.; Nikolov, A. D.; Wasan, D. T., Foaming mechanisms in surfactant free particle suspensions. *AIChE Journal* **2002,** *48* (10), 2307-2314.

40. Safouane, M.; Langevin, D.; Binks, B. P., Effect of Particle Hydrophobicity on the Properties of Silica Particle Layers at the Air−Water Interface. *Langmuir* **2007,** *23* (23), 11546-11553.

41. Liu, Q.; Qu, H.; Liu, S.; Zhang, Y.; Zhang, S.; Liu, J.; Peng, B.; Luo, D., Modified Fe3O4 Nanoparticle Used for Stabilizing Foam Flooding for Enhanced Oil Recovery. *Colloids and Surfaces A: Physicochemical and Engineering Aspects* **2020,** *605*, 125383.

42. Worthen, A. J.; Bagaria, H. G.; Chen, Y.; Bryant, S. L.; Huh, C.; Johnston, K. P., Nanoparticle-stabilized carbon dioxide-in-water foams with fine texture. *Journal of Colloid and Interface Science* **2013,** *391*, 142-151.

43. Geng, D.; Li, J.; Li, H.; Huang, W., Effects of Particle Combinations With Different Wettability on Foam Structure and Stability. *Frontiers in Materials* **2021,** *8*.

44. Hunter, T.; Pugh, R.; Franks, G.; Jameson, G., The role of particles in stabilising foams and emulsions. *Advances in colloid and interface science* **2008,** *137*, 57-81.

45. Amani, P.; Miller, R.; Javadi, A.; Firouzi, M., Pickering foams and parameters influencing their characteristics. *Advances in Colloid and Interface Science* **2022,** *301*, 102606.

46. Manga, M. S.; Hunter, T. N.; Cayre, O. J.; York, D. W.; Reichert, M. D.; Anna, S. L.; Walker, L. M.; Williams, R. A.; Biggs, S. R., Measurements of Submicron Particle Adsorption and Particle Film Elasticity at Oil–Water Interfaces. *Langmuir* **2016,** *32* (17), 4125-4133.

47. Hu, N.; Li, Y.; Wu, Z.; Lu, K.; Huang, D.; Liu, W., Foams stabilization by silica nanoparticle with cationic and anionic surfactants in column flotation: Effects of particle size. *Journal of the Taiwan Institute of Chemical Engineers* **2018,** *88*, 62-69.

48. Gmoser, R.; Bordes, R.; Nilsson, G.; Altskär, A.; Stading, M.; Lorén, N.; Berta, M., Effect of dispersed particles on instant coffee foam stability and rheological properties. *European Food Research and Technology* **2017,** *243*.

49. Zheng, B.; Zheng, B.; Carr, A. J.; Yu, X.; McClements, D. J.; Bhatia, S. R., Emulsions stabilized by inorganic nanoclays and surfactants: Stability, viscosity, and implications for applications. *Inorganica Chimica Acta* **2020,** *508*, 119566.

50. Ozdemir, O.; Hampton, M.; Nguyen, A., Formation and stability of foams stabilized by fine particles with similar size, contact angle and different shapes. *Colloids and Surfaces A-physicochemical and Engineering Aspects - COLLOID SURFACE A* **2011,** *382*, 132-138.

51. Sun, X.; Chen, Y.; Zhao, J., Highly stable aqueous foams generated by fumed silica particles hydrophobised in situ with a quaternary ammonium gemini surfactant. *RSC Advances* **2016,** *6* (45), 38913-38918.

52. Shojaei, M. J.; Méheust, Y.; Osman, A.; Grassia, P.; Shokri, N., Combined effects of nanoparticles and surfactants upon foam stability. *Chemical Engineering Science* **2021,** *238*, 116601.

53. Da, C.; Chen, X.; Zhu, J.; Alzobaidi, S.; Garg, G.; Johnston, K. P., Elastic gas/water interface for highly stable foams with modified anionic silica nanoparticles and a like-charged surfactant. *Journal of Colloid and Interface Science* **2022,** *608*, 1401-1413.

54. Wang, J.; Ye, Z.; Lai, N.; Huang, Y.; Xu, H., Foam stabilized by SiO2/AOS adsorbed at the gas–liquid interface: influence of the degree of nanoparticle modification. *Energy Sources, Part A: Recovery, Utilization, and Environmental Effects* **2021**, 1-15.

55. Maestro, A.; Rio, E.; Drenckhan, W.; Langevin, D.; Salonen, A., Foams stabilised by mixtures of nanoparticles and oppositely charged surfactants: relationship between bubble shrinkage and foam coarsening. *Soft Matter* **2014,** *10* (36), 6975-6983.

56. Zhu, J.; Yang, Z.; Li, X.; Hou, L.; Xie, S., Experimental study on the microscopic characteristics of foams stabilized by viscoelastic surfactant and nanoparticles. *Colloids and Surfaces A: Physicochemical and Engineering Aspects* **2019,** *572*.

57. Pang, B.; Zhang, H.; Schilling, M.; Liu, H.; Wang, X.; Rehfeldt, F.; Zhang, K., High-Internal-Phase Pickering Emulsions Stabilized by Polymeric Dialdehyde Cellulose-Based Nanoparticles. *ACS Sustainable Chemistry & Engineering* **2020,** *8* (19), 7371-7379.

58. Sheng, Y.; Lin, K.; Binks, B. P.; Ngai, T., Ultra-stable aqueous foams induced by interfacial co-assembly of highly hydrophobic particles and hydrophilic polymer. *Journal of Colloid and Interface Science* **2020,** *579*, 628-636.

59. Worthen, A. J.; Bryant, S. L.; Huh, C.; Johnston, K. P., Carbon dioxide-in-water foams stabilized with nanoparticles and surfactant acting in synergy. *AIChE Journal* **2013,** *59* (9), 3490-3501.

60. Thareja, P.; Ising, B. P.; Kingston, S. J.; Velankar, S. S., Polymer foams stabilized by particles adsorbed at the air/polymer interface. *Macromolecular Rapid Communications* **2008,** *29* (15), 1329-1334.

61. Kostakis, T.; Ettelaie, R.; Murray, B. S., Effect of High Salt Concentrations on the Stabilization of Bubbles by Silica Particles. *Langmuir* **2006,** *22* (3), 1273-1280.

62. Yao, X.; Yi, P.; Zhao, G.; Sun, X.; Dai, C., A Study of the Stability Mechanism of the Dispersed Particle Gel Three-Phase Foam Using the Interfacial Dilational Rheology Method. *Materials* **2018,** *11* (5), 699.

63. Worthen, A. J.; Parikh, P. S.; Chen, Y.; Bryant, S. L.; Huh, C.; Johnston, K. P., Carbon Dioxide-in-Water Foams Stabilized with a Mixture of Nanoparticles and Surfactant for CO2 Storage and Utilization Applications. *Energy Procedia* **2014,** *63*, 7929-7938.

64. Bharti, B., Ma, Y., Wu, Y., Shelton, W. A. Jr., Lee, J. G., Self-Assembly and Foaming in Mixtures of Fatty Acid and Silica Nanoparticles. **2020**.

65. Yegya Raman, A. K., Aichele, C. P., The Influence of Nanoparticle Morphology on Surfactant-Nanoparticle Interactions in Emulsions. **2018**.

66. Sun, Q.; Li, Z.; Wang, J.; Li, S.; Li, B.; Jiang, L.; Wang, H.; Lü, Q.; Zhang, C.; Liu, W., Aqueous foam stabilized by partially hydrophobic nanoparticles in the presence of surfactant. *Colloids and Surfaces A: Physicochemical and Engineering Aspects* **2015,** *471.*

67. Bai, T.; Jiang, W.; Chen, y.; Yan, F.; Xu, Z.; Fan, Y., Effect of Multiple Factors on Foam Stability in Foam Sclerotherapy. *Scientific Reports* **2018,** *8*.

68. Yamaguchi, M.; Kanoh, C.; Seemork, J.; Nobukawa, S.; Yanase, K., Effect of Foaming Method on Mechanical Properties of Aqueous Foams Prepared from Surfactant Solution. *Industrial & Engineering Chemistry Research* **2012,** *51* (44), 14408-14413.

69. Dollet, B.; Raufaste, C., Rheology of aqueous foams. *Comptes Rendus Physique* **2014,** *15* (8), 731-747.

70. Cohen-Addad, S.; Höhler, R., Rheology of foams and highly concentrated emulsions. *Current Opinion in Colloid & Interface Science* **2014,** *19* (6), 536-548.

71. Kaganyuk, M.; Mohraz, A., Shear-induced deformation and interfacial jamming of solid-stabilized droplets. *Soft Matter* **2020,** *16* (18), 4431-4443.

72. Van Hooghten, R.; Blair, V. E.; Vananroye, A.; Schofield, A. B.; Vermant, J.; Thijssen, J. H. J., Interfacial Rheology of Sterically Stabilized Colloids at Liquid Interfaces and Its Effect on the Stability of Pickering Emulsions. *Langmuir* **2017,** *33* (17), 4107-4118.

73. Madivala, B.; Fransaer, J.; Vermant, J., Self-Assembly and Rheology of Ellipsoidal Particles at Interfaces. *Langmuir* **2009,** *25* (5), 2718-2728.

74. Cicuta, P.; Stancik, E. J.; Fuller, G. G., Shearing or Compressing a Soft Glass in 2D: Time-Concentration Superposition. *Physical Review Letters* **2003,** *90* (23), 236101.

75. Razavi, S.; Cao, K. D.; Lin, B.; Lee, K. Y. C.; Tu, R. S.; Kretzschmar, I., Collapse of Particle-Laden Interfaces under Compression: Buckling vs Particle Expulsion. *Langmuir* **2015,** *31* (28), 7764-7775.

76. Basavaraj, M. G.; Fuller, G. G.; Fransaer, J.; Vermant, J., Packing, Flipping, and Buckling Transitions in Compressed Monolayers of Ellipsoidal Latex Particles. *Langmuir* **2006,** *22* (15), 6605-6612.

77. Benjamins, J.; Lucassen-Reynders, E. H., Surface dilational rheology of proteins adsorbed at air/water and oil/water interfaces. In *Studies in Interface Science*, Möbius, D.; Miller, R., Eds. Elsevier: 1998; Vol. 7, pp 341-384.

78. Derkach, S.; Krägel, J.; Miller, R., Methods of Measuring Rheological Properties of Interfacial Layers (Experimental Methods of 2D Rheology). *Colloid Journal* **2009,** *71*, 1-17.

79. Pitois, O.; Rouyer, F., Rheology of particulate rafts, films, and foams. *Current Opinion in Colloid & Interface Science* **2019,** *43*, 125-137.

80. Yu, K.; Zhang, H.; Biggs, S.; Xu, Z.; Cayre, O. J.; Harbottle, D., The rheology of polyvinylpyrrolidone-coated silica nanoparticles positioned at an air-aqueous interface. *Journal of Colloid and Interface Science* **2018,** *527*, 346-355.

81. Firouzi, M.; Kovalchuk, V. I.; Loglio, G.; Miller, R., Salt effects on the dilational viscoelasticity of surfactant adsorption layers. *Current Opinion in Colloid & Interface Science* **2022,** *57*, 101538.

82. Yue, L.; Pu, W.; Zhao, T.; Zhuang, J.; Zhao, S., A high performance magnetically responsive Janus nano-emulsifier: Preparation, emulsification characteristics, interfacial rheology, and application in emulsion flooding. *Journal of Petroleum Science and Engineering* **2022,** *208*, 109478.

83. Maestro, A.; Deshmukh, O. S.; Mugele, F.; Langevin, D., Interfacial Assembly of Surfactant-Decorated Nanoparticles: On the Rheological Description of a Colloidal 2D Glass. *Langmuir* **2015,** *31* (23), 6289-6297.

84. Zhu, J.; Da, C.; Chen, J.; Johnston, K. P., Ultrastable N2/Water Foams Stabilized by Dilute Nanoparticles and a Surfactant at High Salinity and High Pressure. *Langmuir* **2022**.

85. Hermans, E.; Vermant, J., Interfacial shear rheology of DPPC under physiologically relevant conditions. *Soft Matter* **2014,** *10* (1), 175-186.

86. Karperien, A. *FracLac for ImageJ*, 1999-2013.

87. Quéré, D., Wetting and roughness. *Annual review of materials research* **2008,** *38* (1), 71-99.

88. Della Volpe, C.; Penati, A.; Peruzzi, R.; Siboni, S.; Toniolo, L.; Colombo, C., The combined effect of roughness and heterogeneity on contact angles: the case

of polymer coating for stone protection. *Journal of Adhesion Science and Technology* **2000,** *14* (2), 273-299.

89. Drelich, J.; Miller, J. D., The Effect of Solid Surface Heterogeneity and Roughness on the Contact Angle/Drop (Bubble) Size Relationship. *Journal of Colloid and Interface Science* **1994,** *164* (1), 252-259.

90. CHAPTER 4 - Foam Drilling. In *Underbalanced Drilling: Limits and Extremes*, Rehm, B.; Haghshenas, A.; Paknejad, A.; Al-Yami, A.; Hughes, J.; Schubert, J., Eds. Gulf Publishing Company: 2012; pp 197-295.

91. Smith, W. E.; Zukoski, C. F., Role of solvation forces in the gelation of fumed silica–alcohol suspensions. *Journal of Colloid and Interface Science* **2006,** *304* (2), 348-358.

92. Feitosa, K.; Marze, S.; Saint-Jalmes, A.; Durian, D., Electrical conductivity of dispersions: From dry foams to dilute suspensions. *Journal of Physics: Condensed Matter* **2005,** *17*.

93. Forel, E.; Rio, E.; Schneider, M.; Beguin, S.; Weaire, D.; Hutzler, S.; Drenckhan, W., The surface tells it all: relationship between volume and surface fraction of liquid dispersions. *Soft Matter* **2016,** *12* (38), 8025-8029.

94. Maestro, A.; Drenckhan, W.; Rio, E.; Höhler, R., Liquid dispersions under gravity: volume fraction profile and osmotic pressure. *Soft Matter* **2013,** *9* (8), 2531-2540.

95. Kabalnov, A.; Weers, J., Kinetics of Mass Transfer in Micellar Systems: Surfactant Adsorption, Solubilization Kinetics, and Ripening. *Langmuir* **1996,** *12* (14), 3442-3448.

96. Santos, J.; Calero, N.; Trujillo-Cayado, L. A.; Garcia, M. C.; Muñoz, J., Assessing differences between Ostwald ripening and coalescence by rheology, laser diffraction and multiple light scattering. *Colloids Surf B Biointerfaces* **2017,** *159*, 405-411.

97. Benrabah, L.; Kemel, K.; Twarog, C.; Huang, N.; Solgadi, A.; Laugel, C.; Faivre, V., Lipid-based Janus nanoparticles for pharmaceutical and cosmetic applications: Kinetics and mechanisms of destabilization with time and temperature. *Colloids Surf B Biointerfaces* **2020,** *195*, 111242.

98. Wagner, C., Theorie der Alterung von Niederschlägen durch Umlösen (Ostwald-Reifung). *Zeitschrift für Elektrochemie, Berichte der Bunsengesellschaft für physikalische Chemie* **1961,** *65* (7-8), 581-591.

99. Lifshitz, I. M.; Slyozov, V. V., The kinetics of precipitation from supersaturated solid solutions. *Journal of Physics and Chemistry of Solids* **1961,** *19* (1), 35-50.

100. Gibbs, J. W., *The scientific papers of J. Willard Gibbs*. Ox Bow, Woodbridge: 1993.

101. Correia, E. L.; Brown, N.; Ervin, A.; Papavassiliou, D. V.; Razavi, S., Contamination in Sodium Dodecyl Sulfate Solutions: Insights from the Measurements of Surface Tension and Surface Rheology. *Langmuir* **2022,** *38* (23), 7179-7189.

102. Freer, E. M.; Wong, H.; Radke, C. J., Oscillating drop/bubble tensiometry: Effect of viscous forces on the measurement of interfacial tension. *Journal of colloid and interface science* **2005,** *282*, 128-32.

103. Berry, J. D.; Neeson, M. J.; Dagastine, R. R.; Chan, D. Y. C.; Tabor, R. F., Measurement of surface and interfacial tension using pendant drop tensiometry. *Journal of Colloid and Interface Science* **2015,** *454*, 226-237.

104. Renggli, D.; Alicke, A.; Ewoldt, R. H.; Vermant, J., Operating windows for oscillatory interfacial shear rheology. *Journal of Rheology* **2020,** *64* (1), 141-160.

Appendix I.

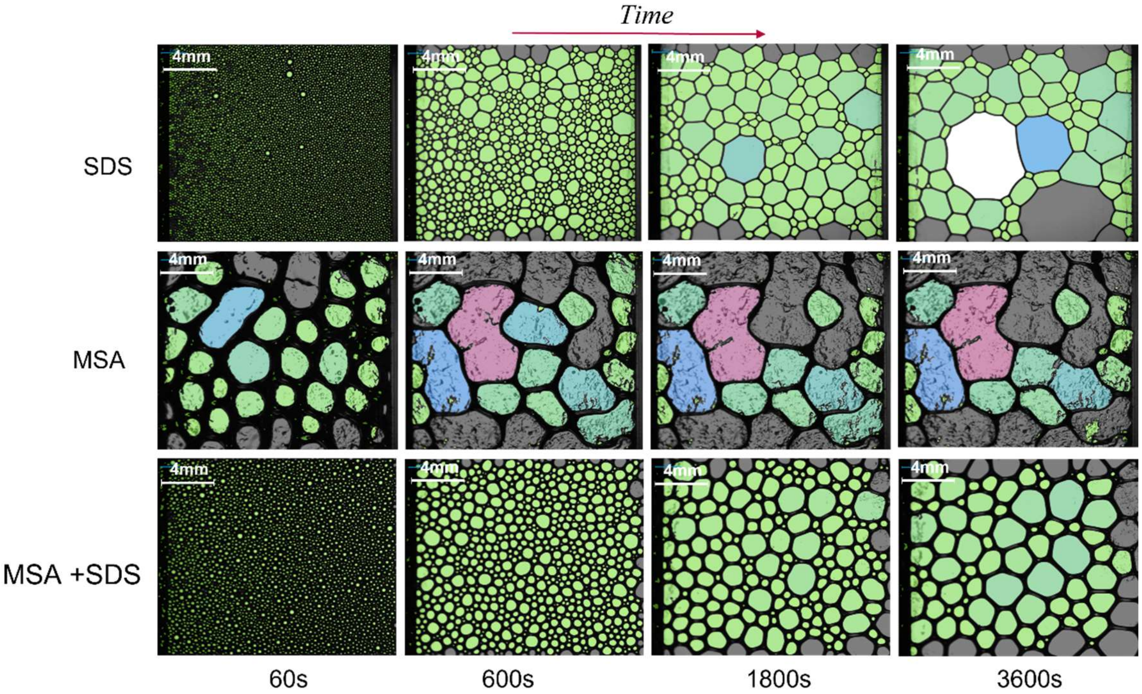

Figure A.1. Comparison of mixed system foams. Row 1) 0.5 CMC SDS at 60, 600, 1800, and 3600s respectively; Row 2) 2.0wt.% MSA at 60, 600, 1800, and 3600s respectively; Row 3) Mixed MSA & 0.5 CMC SDS at 60, 600, 1800, and 3600s respectively.

Shown in Fig. A.1 are the microstructure images of 0.5 CMC SDS, 2.0wt.% MSA, and the mixed system of 0.5 CMC SDS/2.0wt.% MSA. It can be noticed that the mixed foam microstructure resembled the SDS only system initially with the multitude of small bubbles which is unlike the particle foams and remained smaller and more circular than the MSA microstructure altogether. The drainage was reduced significantly visually, as the foam lamellae in the mixed foam was much thicker and more resembled the MSA lamellae. While the shape and size resulted from the larger surfactant number at the interface, because the MSA particles were able to create a network the drainage was slowed, and the overall destabilization was less than pure SDS systems.

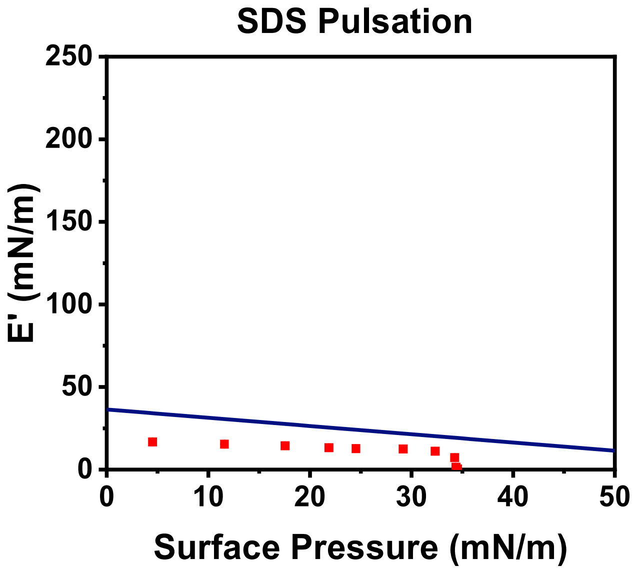

Figure A.2. SDS elastic modulus values (red points), with regards to the Gibbs stability criterion (blue line).

Fig. A.2 showed the low E' values obtained from the surfactant-packed interface. All values are less than what were obtained of the colloidal and MSA interfaces shown in Fig. 6.3, which correlated with the low stability of the surfactant foams to resist any types of deformation such as coalescence or Ostwald ripening. This was made clearer by the data being below the Gibbs stability criterion, which further showed that the interface was poorly suited to resist Ostwald ripening and was ultimately unstable after foam generation.

Worthington and Bond Number

One topic that had to be broached was whether the tensiometry data shown above was accurate, and within the limits of the apparatus. To understand this, the Worthington number (Wo) and Bond number (Bo) were calculated.[103] The Worthington and Bond numbers can be shown as follows:

$$Wo = \frac{\Delta\rho g V_d}{\pi\gamma D_n} \Rightarrow \frac{V_d}{\gamma} \qquad Bo = \frac{\Delta\rho g L^2}{\gamma} \tag{8}$$

Where $\Delta\rho$ is the difference in density of the two phases, in this case air and water, g is gravity (9.8ms^{-2}), V_d is the volume of the drop (L), γ is the surface tension measured (N*m^{-1}), D_n is the diameter of needle being used (m), and L is the characteristic length in this case being the radii of the droplet (m). What could be seen was that density, gravity, Pi, and the needle diameter can all be taken as constants in Wo, leaving Wo as a function of drop volume and surface tension only. There can be two ways to interpret the Wo as well, a static or a dynamic version depending on whether the surface tension measured changed with the drop volume. Both Wo and Bo are used to understand whether the interfacial or gravitational forces are more dominant on the system, with the Worthington number being a more applicable scale with a defined range from 0 to 1. Any data with Wo > 0.25 was deemed useable and accurate with gravitational forces still being present which caused a drop shape to develop, and discarded trials that would fall below this limit. Shown below in Fig. A.3 was the Wo for the same MSA trial with either a static or dynamic surface tension being used in calculation. It can be easily seen the difference between which surface tension is used, as the static surface tension eventually leads to very low Wo values while the dynamic value maintained a relatively steady Wo around 0.55 and began to increase at lower surface areas. This increase was due to the volume of the drop, and therefore the surface area, changing at a faster rate than the surface tension which led to Wo expression increasing in value compared to the static which can only decline due to only being a function of drop volume. So, depending on whether the surface tension, and therefore Wo, was taken as static or dynamic could very easily change which experimental results were considered accurate and which were not. Due to the surface tension ultimately changing with drop volume, the dynamic Wo value was utilized for all trials.

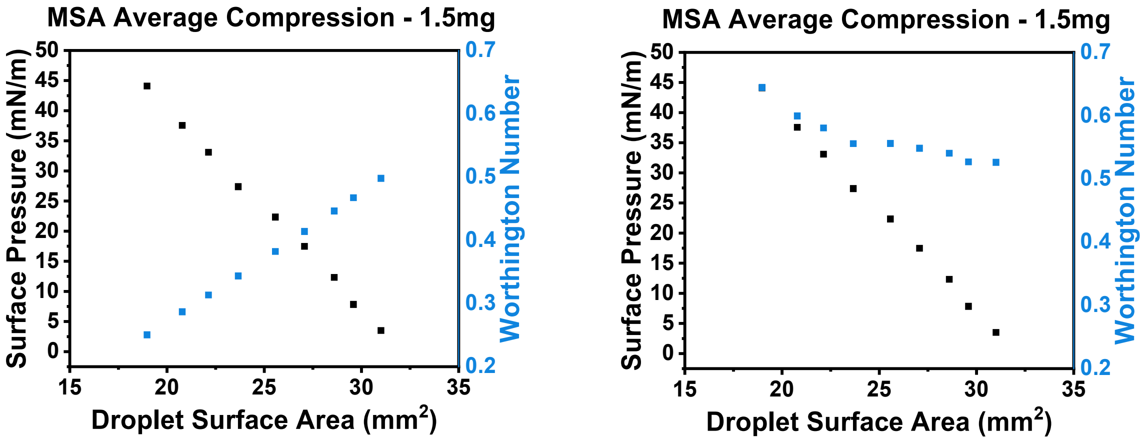

Figure A.3. Static (left) and dynamic (right) Wo values for the same MSA compression data set.

The raw phase angle (δ) was also used to analyze the data sets, as viscoelastic samples have angles of 0º < δ < 90º, which falls into the range between fully viscous or fully elastic materials. The data points with δ > 90º must be looked at carefully as they are not physically valid.

Shear Rheology Limits

To properly understand which data could be considered reliable and which had to be taken with caution, Vermant et al. determined three separate limits that could be applied to the data retrieved from the interfacial shear experiments.[104] Shown below, the first major limit was similar to one seen using the tensiometer, which was that the raw phase angle δ must be greater than 0º and less than 90º as those are the bounds for a completely solid or a completely viscous material, respectively. The second limit used to evaluate the rheological data was to determine the ratio of measured oscillatory torque to the instrument limitation for oscillatory torque. Oscillatory torque was the torque require to rotate the ring at the interface, so if the ratio of torques was too low that indicated that the trial was almost outside of the instrument limitations and that the data obtained could be influenced by the geometry. Lastly, the ratio of measured oscillatory stress to the instruments limitation of oscillatory stress could be determined. This ratio considered the inertial effects of both the geometry and the rheometer, so as the stress ratio decreased, the system approached a regime in which the stress recorded could be due to the instruments and not the sample which would correspond to erroneous data. There are three separate cases of limits than can be obtained shown below the criteria which correspond to if the data can be assumed good data or if it needs to be taken with care. For each case, the raw phase angle must stay between 0º and 90º, or else the data point must be considered with caution. If both the ratios of torque and stress are greater than 10 then the data point was considered trustworthy, if one was > 10 and the other was > 5 it was a plausible data point, and if one of them was < 5 then that point must also be used with caution. These limits were applied to each trial in order to better understand which data points could be trusted and ultimately led to the minimum and maximum frequencies used during sweeps of 0.1 Hz and 10 Hz, respectively.

$$0° < \delta < 90° \tag{9}$$

$$X_{Osc.\ Torque} = \frac{M_{Measured}}{M_{Instr.\ Limit}} > 10 \quad (Good) \tag{10a}$$

$$X_{Osc.\ Torque} = \frac{M_{Measured}}{M_{Instr.\ Limit}} > 5 \quad (Plausible) \tag{10b}$$

$$X_{Osc.\ Torque} = \frac{M_{Measured}}{M_{Instr.\ Limit}} < 5 \quad (Use\ with\ care) \tag{10c}$$

$$X_{Osc.\ Stress} = \frac{|G_S^*|}{\frac{C_M}{C_\Theta} I\omega^2} > 10 \quad (Good) \tag{11a}$$

$$X_{Osc.\ Stress} = \frac{|G_S^*|}{\frac{C_M}{C_\Theta} I\omega^2} > 5 \quad (Plausible) \tag{11b}$$

$$X_{Osc.\ Stress} = \frac{|G_S^*|}{\frac{C_M}{C_\Theta} I \omega^2} < 5 \qquad (Use\ with\ care) \tag{11c}$$